A&A 488, 579–595 (2008)
DOI: 10.1051/0004-6361:200809798

Astronomy & Astrophysics

Evolution of massive protostars: the IRAS 18151–1208 region⋆,⋆⋆

M. Marseille[1,2], S. Bontemps[1,2], F. Herpin[1,2], F. F. S. van der Tak[3], and C. R. Purcell[4]

[1] Université Bordeaux 1, Laboratoire d'Astrophysique de Bordeaux, 2 rue de l'Observatoire, 33270 Bordeaux, France
e-mail: [marseille;bontemps;herpin]@obs.u-bordeaux1.fr
[2] CNRS/INSU, UMR 5804, BP 89, 33270 Floirac, France
[3] SRON Netherlands Institute for Space Research, Landleven 12, 9747 AD Groningen, The Netherlands
e-mail: vdtak@sron.nl
[4] University of Manchester, Jodrell Bank Observatory, Macclesfield, Cheshire SK11 9DL, UK
e-mail: Cormac.Purcell@manchester.ac.uk

Received 18 March 2008, Accepted 3 June 2008

ABSTRACT

Context. The study of physical and chemical properties of massive protostars is critical for better understanding the evolutionary sequence that leads to the formation of high-mass stars.
Aims. IRAS 18151–1208 is a nearby massive region (d = 3 kpc, $L \sim 2 \times 10^4\ L_\odot$) that splits into three cores: MM1, MM2, and MM3 (separated by 1′–2′). We aim at (1) studying the physical and chemical properties of the individual MM1, MM2, and MM3 cores; (2) deriving their evolutionary stages; (3) using these results to improve our view of the evolutionary sequence of massive cores.
Methods. The region was observed in the CS, $C^{34}S$, H_2CO, HCO^+, $H^{13}CO^+$, and N_2H^+ lines at mm wavelengths with the IRAM 30 m and Mopra telescopes. We use 1D and 2D modeling of the dust continuum to derive the density and temperature distributions, which are then used in the RATRAN code to model the lines and constrain the abundances of the observed species.
Results. All the lines were detected in MM1 and MM2. MM3 shows weaker emission, or is even undetected in HCO^+ and all isotopic species. MM2 is driving a newly discovered CO outflow and hosts a mid-IR-quiet massive protostar. The abundance of CS is significantly greater in MM1 than in MM2, but smaller than in a reference massive protostar such as AFGL 2591. In contrast, the N_2H^+ abundance decreases from MM2 to MM1, and is larger than in AFGL 2591.
Conclusions. Both MM1 and MM2 host an early-phase massive protostar, but MM2 (and mid-IR-quiet sources in general) is younger and dominated more by the host protostar than MM1 (mid-IR-bright). The MM3 core is probably in a pre-stellar phase. We find that the $N_2H^+/C^{34}S$ ratio varies systematically with age in the massive protostars for which the data are available. It can be used to identify young massive protostars.

Key words. ISM: individual objects: IRAS 18151–1208 – ISM: abundances – stars: formation – line: profiles

1. Introduction

How high-mass stars form is still an open issue (e.g. Zinnecker & Yorke 2007). It is particularly unclear whether the formation process for OB/high-mass stars is different from the way solar-types or low-mass stars form. Stars more massive than ∼10 $M_\odot$ may form like a scaled-up version (high accretion rates) of the single (or monolithic) collapse observed for the low-mass stars, or else require a more complex process in which competitive accretion inside the central regions of a forming cluster may play a decisive role (e.g. Bonnell et al. 2004). In the first scenario, the observed high-mass clumps (100 to 1000 $M_\odot$; 0.5 pc in size) are expected to fragment to form self-gravitating high-mass cores (10 to 100 $M_\odot$; 0.01–0.1 pc in size; e.g. Krumholz et al. 2007), which would collapse individually to form massive single or binary stars. In the second scenario, the competitive accretion is expected to occur inside the high-mass clumps. The study of the properties of high-mass clumps is therefore a central observational issue in our understanding of the earliest phases of high-mass star formation.

From a selection of IRAS sources not associated with any bright radio source but having the IRAS colors of UC-HII regions (as defined by Wood & Churchwell 1989), Sridharan et al. (2002) have built a sample of so-called high-mass protostellar objects (hereafter HMPOs), which would correspond to the pre-UC-HII phase of the formation of high-mass stars. Beuther et al. (2002b) found that the HMPOs were systematically associated with massive clumps as detected in the dust continuum and in CS line emission. These clumps correspond to the earliest phases of high-mass star formation. They have not yet formed any bright HII regions and contain a large amount of gas at high densities. The precise evolutionary stages of the individual HMPOs might, however, be very diverse, and they require being derived individually through dedicated, detailed studies.

Recently, Motte et al. (2007) have investigated the whole Cygnus X complex and obtained a first unbiased view of the evolutionary scheme for high-mass clumps and cores. Like for HMPOs, the massive clumps (∼0.5 pc in size) in Cygnus X could be resolved into massive cores (∼0.1 pc). Roughly half of these cores have been found to be very bright in the (mid)-infrared

⋆ Observed with the IRAM 30 m and Mopra telescopes. IRAM is supported by INSU/CNRS (France), MPG (Germany) and IGN (Spain). The Mopra telescope is part of the Australia Telescope, which is funded by the Commonwealth of Australia for operation as a National Facility managed by CSIRO.

⋆⋆ Channel maps in FITS format of Fig. 2 are available in electronic form at the CDS via anonymous ftp to cdsarc.u-strasbg.fr (130.79.128.5) or via http://cdsweb.u-strasbg.fr/cgi-bin/qcat?J/A+A/488/579

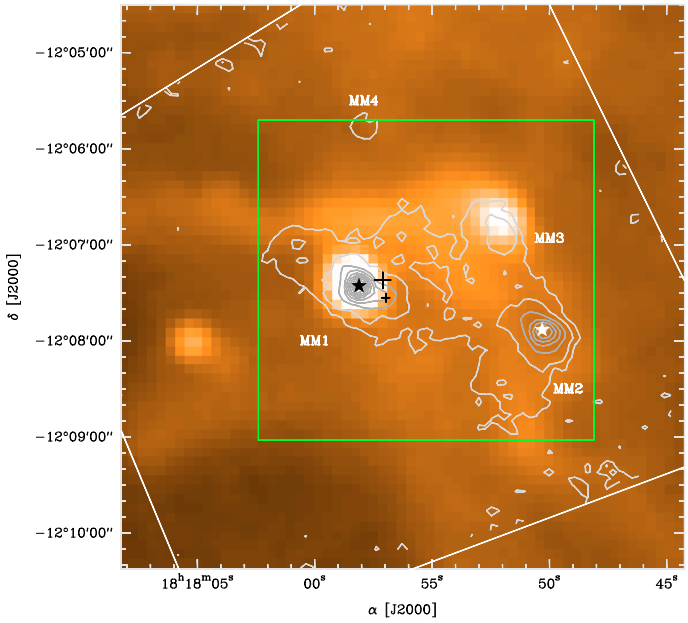

Fig. 1. Image of the MSX 8 μm emission toward IRAS 18151–1208 (color scale) overlaid with the 1.2 mm map (white polygon) by Beuther et al. (2002b) (white contours at 5 and 10%, and grey contours from 20% to 90% of the maximum). The large and small crosses indicate the positions of the IRAS source and of MM1-SW (see text), respectively. The black and white star symbols show the positions of the methanol and water masers, respectively. The green polygon displays the region mapped in the present study (see Fig. 2).

(such as AFGL 2591; e.g. van der Tak et al. 1999) and therefore very luminous: the mid-IR high-luminosity massive cores. The other half are either weak or not detected at all in the mid-IR, hereafter the mid-IR-quiet massive cores. Surprisingly, all the mid-IR-quiet massive cores were, however, found to drive powerful SiO outflows. They could therefore be safely understood as the precursors of the infrared high-luminosity massive cores.

IRAS 18151–1208 is a rather typical ($L \sim 10^4\ L_\odot$) and relatively nearby (3 kpc) HMPO (Sridharan et al. 2002). Beuther et al. (2002b) show that the clump actually splits into four individual cores MM1, MM2, MM3, and MM4 (see Fig. 1 for an overview of the region). In addition, MM1 seems to further split into two cores, separated by 16″. We hereafter refer to MM1-SW for the secondary peak to the southwest of MM1, which possibly hosts an embedded protostar (Davis et al. 2004). The weakest core MM4 is clearly outside the main region, hence it will not be considered in this paper. A CO outflow toward MM1 was discovered by Beuther et al. (2002c). The MM1 and MM2 cores are roughly two times larger, and have similar masses (using the same dust emissivity and temperature) to the most massive cores in Motte et al. (2007). The IRAS source coincides with MM1, and no significant IRAS contribution can be safely attributed to MM2 or MM3. MM3 is the least massive and compact core and could actually still be a quiescent or pre-stellar core. The IRAS 18151–1208 region is therefore particularly interesting to study since it hosts three individual cores that could be interpreted as high-mass star formation sites in three different evolutionary stages. Millimeter and sub-millimeter wave observations are reported in McCutcheon et al. (1995) and Beuther et al. (2002b). The near-IR counterparts (H_2 jets and HH objects) of the CO outflow driven by MM1 have been imaged by Davis et al. (2004).

Table 1. IRAS 18151–1208 sources characteristics, showing offsets from IRAS position, J2000 coordinates, and velocity in the local standard of rest (Beuther et al. 2002b).

source	$\Delta\alpha$[″]	$\Delta\delta$[″]	α[J2000]	δ[J2000]	v [km s^{-1}]
MM1	13.2	–4.9	$18^h17^m58.0^s$	–12°07′27″	33.4
MM2	–98.9	–32.8	$18^h17^m50.4^s$	–12°07′55″	29.7
MM3	–72.3	26.5	$18^h17^m52.2^s$	–12°06′56″	30.7

Molecular line observations compared with results of line modeling based on a physical model of the source is a classical technique for constraining the physical and chemical properties of protostellar objects (see Ceccarelli et al. 1996; van der Tak 2005, for a review). While different approaches can be adopted, the most reliable and most often used method consists in constraining first the physical (density and temperature distributions) model from the dust continuum emission (mid-IR to millimeter wavelengths), and then using this physical model to derive the fractional abundances of molecular species from line-emission modeling (van der Tak et al. 1999; Hogerheijde & van der Tak 2000; Schöier et al. 2002; Belloche et al. 2002; Hatchell & van der Tak 2003). Due to the dramatic changes in physical conditions inside the protostellar envelopes (increase in density and temperature, radiation, shocks), chemical evolution is observed and can be modeled thanks to chemical network codes. It is even expected that chemistry could provide a reliable clock for dating protostellar objects (e.g. van Dishoeck & Blake 1998; Doty et al. 2002; Wakelam et al. 2004).

After the description of the molecular observations and of the continuum data from the literature (Sect. 2), the results are presented in Sect. 3. Section 4 gives the modeling procedure from the fits of the spectral energy distributions (hereafter SEDs) for MM1 and MM2 using MC3D[1] code (Sects. 4.1.1 and 4.2.1) to the non-LTE calculations of the line profiles and intensities for all observed molecules using RATRAN[2] code (Sects. 4.1.2, 4.1.3, 4.2.2, and 4.2.3). In Sect. 5, we discuss the results of this detailed analysis in order to improve our observational view of the evolution of high-mass cores from pre-stellar to high-luminosity massive protostars.

2. Observations

Observations were performed during two sessions. The first one in June 2005 at Mopra, the 22 m dish of the Australia Telescope National Facility[3] (ATNF). The second was in August 2005 at Pico Veleta, on the IRAM 30 m antenna[4].

2.1. Mopra observations

The IRAS 18151–1208 region was mapped in the on-the-fly (OTF) mode in the rotational transition of CS (J = 2–1) at 98.0 GHz, $C^{34}S$ (J = 2–1) at 96.4 GHz , HCO^+ (J = 1–0) at 89.2 GHz, $H^{13}CO^+$ (J = 1–0) at 86.8 GHz, and N_2H^+ (J = 1–0) at 93.2 GHz. Each run covered a field of 5′ × 5′ with a half-power beam width (HPBW) of approximatively 36″ ($\eta_{\rm mb}$ = 0.49) and sampled with a $\Delta\theta$ step of 9″. We used the 3 mm receiver of the ATNF telescope with the digital auto-correlator set to the 64 MHz bandwidth with 1024

[1] See Wolf et al. (1999) for details.
[2] See van der Tak et al. (1999, 2000a) for details.
[3] http://www.narrabri.atnf.csiro.au/mopra/
[4] http://iram.fr/IRAMES/index.htm

Table 2. List of observational parameters for IRAM 30 m and 22 m Mopra telescopes.

Species	Transition	Frequency [GHz]	HPBW [″]	Instrument[d]	η_{mb}	Receiver	δv [m s^{-1}]	Mode	T_{sys} [K]
CS	J = 2–1	97.9809	25	30 m	0.78	A100	60	RaM[a]	260
	J = 2–1	97.9809	32	Mo	0.49	3.5 mm	191	OTF[c]	240
	J = 3–2	146.9690	17	30 m	0.69	D150	80	RaM[a]	420
	J = 5–4	244.9356	10	30 m	0.49	D270	96	RaM[a]	1150
$C^{34}S$	J = 2–1	96.4129	25	30 m	0.78	A100	61	RaM[a]	190
	J = 2–1	96.4129	32	Mo	0.49	3.5 mm	194	OTF[c]	~270
	J = 3–2	144.6171	17	30 m	0.69	D150	81	RaM[a]	390
CO	J = 2–1	230.5380	11	30 m	0.52	HERA	406	RaM2[b]	~600
H_2CO	$J = 3_{03}$–2_{02}	218.2222	11	30 m	0.54	HERA	107	RaM2[b]	250
	$J = 3_{22}$–2_{21}	218.4756	11	30 m	0.54	HERA	107	RaM2[b]	250
	$J = 3_{12}$–2_{11}	225.6978	11	30 m	0.53	A230	104	RaM[a]	870
HCO^+	J = 1–0	89.1885	36	Mo	0.49	3.5 mm	210	OTF[c]	~260
$H^{13}CO^+$	J = 1–0	86.7542	36	Mo	0.49	3.5 mm	216	OTF[c]	~175
N_2H^+	J = 1–0	93.1737	36	Mo	0.49	3.5 mm	201	OTF[c]	~180

Note: Cols. 2–10 indicate energy level transitions, line emission frequencies, half power beam width (HPBW), instrument (30 m for IRAM-30 m and Mo for Mopra telescope), main beam efficiency η_{mb}, receiver name, velocity resolution δv, observation mode, and system temperature T_{sys}.
[a] RaM – Raster Map mode set to create a 3 × 3 pixels mini-map with a $\Delta\theta$ step of 10″ around source emission peak.
[b] RaM2 – Raster Map mode with HERA receiver, set to create a 190″ × 140″ map with a $\Delta\theta$ step of 6″ towards MM1, MM2, and MM3.
[c] OTF – On-The-Fly observing mode carrying out on a 5′ × 5′ grid with an angle step $\Delta\theta$ of 9″ and an OFF position at 30′ from the center.
[d] Conversional factor is S/T_{mb} = 4.95 Jy/K for IRAM 30 m telescope and S/T_{mb} = 22 Jy/K for ATNF 22 m telescope.

channels and both polarizations. It provides a velocity resolution of ~0.2 km s^{-1} over a 200 km s^{-1} range. Observations happened while the weather was clear, with a system temperature T_{sys} ~ 175–260 K (see Table 2 for details). Pointing and focus adjustments were set on Jupiter or known sources of calibration.

Raw data were reduced with AIPS++ LIVEDATA and GRIDZILLA tasks (McMullin et al. 2004). LIVEDATA performed the subtraction between the SCAN spectra row and the OFF spectrum. Then it fit the baseline with a polynomial. We used the GRIDZILLA package to resample and build a data cube with regular pixel scale, weighted with the system temperature T_{sys}. We created a 39 × 39 grid of 9″ × 9″ pixel size convolved by a Gaussian with an FWHM of 18″, truncated at an angular offset of 36″. Finally, due to positional errors that we found in maps, a shift in α of 14″ for N_2H^+, 10″ for CS and 5″ for HCO^+ was applied to fit millimeter-continuum peak positions of the three sources given by Beuther et al. (2002b).

2.2. IRAM-30 m observations

We observed the rotational transition of CO (J = 2–1) molecule at 230.5 GHz and the two H_2CO rotational para-transitions ($J = 3_{03}$–2_{02}) and ($J = 3_{22}$–2_{21}) respectively at 218.2 GHz and 218.5 GHz simultaneously, using the HERA 3 × 3 pixel dual multi-beam receiver with VESPA backends at a resolution of 160 kHz for CO and 40 kHz for H_2CO. Thus we built two 190″ × 140″ maps sampling every 6″ around MM1, MM2, and MM3. This observation was done while the weather was good (τ_0^{atm} = 0.17), with T_{sys} ~ 600 K and 250 K for CO and H_2CO, respectively. The maps are incomplete because raster mapping was not set to cover the entire $\Delta\alpha$ and $\Delta\delta$, and the HERA vertical polarization (set for the CO) had a dead pixel (number 4). All pointings and focus were set on suitable planets (i.e. Jupiter) or calibration sources.

The IRAS 18151–1208 region was also mapped in the rotational transitions of CS at 98.0, 147.0, and 244.9 GHz (J = 2–1, J = 3–2, J = 5–4), in the isotopic $C^{34}S$ rotational transitions at 96.4 and 144.6 GHz (J = 2–1, J = 3–2) and in the H_2CO rotational ortho-transition ($J = 3_{12}$–2_{11}) at 225.7 GHz, using simultaneously A100, A230, D150, and D270 receivers coupled to the high-resolution VESPA backend (resolution of 80 kHz). Central emission peaks of MM1, MM2, and MM3 were quickly mapped with a 3 × 3 raster position switching method with a step of 10″. Observations happened while sky conditions were reasonable (τ_0^{atm} ~ 0.1–0.6 and T_{sys} ~ 260–1150 K).

Reduction for all IRAM 30 m telescope data were performed with the CLASS software from the GILDAS suite (Guilloteau & Lucas 2000). We found and eliminated unusable data and treated platforming that appeared in CO and H_2CO baselines, then spectra at the same position were summed and finally antenna temperature T_a^* was converted into T_{mb} (see Table 2 for the values of η_{mb}).

3. Results

The modeling of the spectral energy distribution (SED) of a source is a common way to derive its density and temperature profiles (e.g. van der Tak et al. 1999). The obtained so-called physical model is then used as such to derive the abundances and to further investigate the physical properties (kinematics for instance) through the line emission modeling.

We thus observed CS, $C^{34}S$, HCO^+, and $H^{13}CO^+$ line emissions, which are bright and are tracing dense gas. We also observed H_2CO line emission, which traces dense gas and its temperature. In addition, we observed N_2H^+ line emission, which is a cold gas indicator and finally CO that traces molecular gas flows.

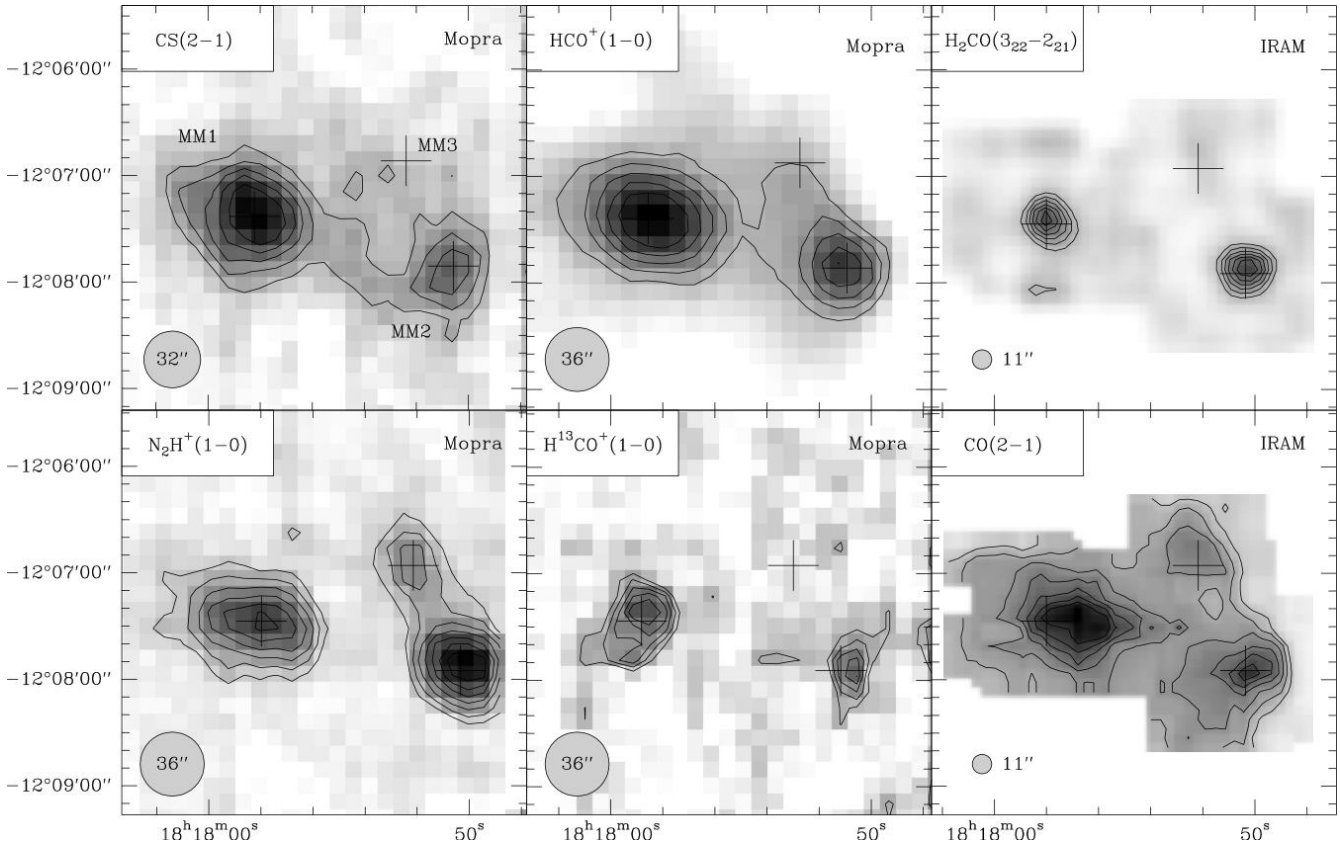

Fig. 2. Integrated velocity maps of CS (2–1), N_2H^+ (1–0), HCO^+ (1–0), $H^{13}CO^+$ (1–0) obtained with the Mopra 22 m telescope (left and middle panels) and CO (2–1), H_2CO (3_{22}–2_{21}) maps obtained with the IRAM 30 m telescope (right panel). Level contours fit 90% to 10% of peak flux with a 10% step. Only levels exceeding the threshold of $2\sigma_{noise}$ in each map are plotted in order to identify detections. Peak fluxes are 16.9 K km s^{-1} for CS, 16.9 K km s^{-1} for N_2H^+, 32.9 K km s^{-1} for HCO^+, 2.31 K km s^{-1} for $H^{13}CO^+$, 21.1 K km s^{-1} for H_2CO, and 393 K km s^{-1} for CO. Crosses indicate the 1.2 mm continuum positions (Beuther et al. 2002b) for the three sources.

Table 3. Sources extension at $3\sigma_{noise}$, minor-to-major axis ratio b/a, and position angle (PA; counterclockwise angle relative to the north) for each molecular transition observed. When the emission is almost spherical ($b/a \geq 0.85$) PA is uncertain and set to 0°.

	MM1			MM2			MM3		
	Ext.	b/a	PA [°]	Ext.	b/a	PA [°]	Ext.	b/a	PA [°]
CO (2–1)	72″ × 51″	0.71	+85	34″ × 23″	0.68	–53	45″ × 36″	0.8	+53
H_2CO (3_{22}–2_{21})	35″ × 30″	0.85	0	35″ × 30″	0.85	0	–	–	–
CS (2–1)	97″ × 81″	0.83	+57	75″ × 62″	0.83	–31	–	–	–
N_2H^+ (1–0)	89″ × 62″	0.69	+77	55″ × 54″	0.98	0	54″ × 52″	0.96	0
HCO^+ (1–0)	104″ × 78″	0.75	+75	57″ × 56″	0.98	0	–	–	–
$H^{13}CO^+$ (1–0)	52″ × 38″	0.73	–28	<*HPBW*	–	–	–	–	–

3.1. Large scale maps: CO (2–1), H_2CO (3_{22}–2_{21}), CS (2–1), HCO^+ (1–0), $H^{13}CO^+$ (1–0), and N_2H^+ (1–0)

The velocity-integrated maps in CO (2–1), H_2CO (3_{22}–2_{21}), CS (2–1), HCO^+ (1–0), $H^{13}CO^+$ (1–0), and N_2H^+ (1–0) are displayed in Fig. 2. Table 3 gives the derived emission extensions (at the $3\sigma_{noise}$ level), the minor-to-major axis ratio b/a, and position angle (PA) of MM1, MM2, and MM3. Note that the $C^{34}S$ (2–1) MOPRA map was too noisy and was discarded.

The molecular emission always peaks at the positions of the three cores (millimeter-continuum peak positions by Beuther et al. 2002b). While MM1 and MM2 are always clearly detected, MM3 seems to be too weak in CS (2–1), H_2CO (3_{22}–2_{21}) and $H^{13}CO^+$ (1–0) to be detected. The emission is extended even between the cores for the CS, HCO^+, and CO lines but are more peaked for N_2H^+, $H^{13}CO^+$, and H_2CO lines. Some chemical differences are already clear in CS, N_2H^+, and H_2CO. While MM1 is generally brighter than MM2, such as in the dust continuum, MM2 has the same intensity in H_2CO and is even significantly brighter in N_2H^+ than MM1.

The CS (2–1) line emission is detected for MM1 and MM2 and weak emission could be present at 1σ for MM3. The MM1 emission is stronger than MM2 and covers a larger area, with extensions of 97″ × 81″ and 75″ × 62″ for MM1 and MM2, respectively. It indicates that a large-scale envelope is surrounding MM1 and MM2. Axis ratios b/a are equal to 0.83 for MM1 and MM2, showing that the emission is almost spherical. The position angle of MM1 emission (+57°) is similar to the position angle of the large dust emission of +62° given by Beuther et al. (2002b). We note that emission is detected between MM1 and MM2. It suggests that they could be connected by a dense molecular filament.

The cold-gas tracer N_2H^+ (1–0) is detected toward the three cores. Emission from MM2 is stronger and more concentrated than for MM1 (89″ × 62″ and 55″ × 54″, respectively), suggesting that MM2 has a smaller and colder envelope. A similar behavior has been observed by Reid & Matthews (2007) for two similar cores in IRAS 23033+5951. The elongation of MM1 (b/a = 0.69) and position angle (+77°) resembles the extension of the dust emission. The MM3 line emission is stronger compared to other molecules and shows a connection with MM2. Together with a similar rest velocity for MM2 and MM3, that confirms that MM3 belongs to the IRAS 18151–1208 region.

The HCO^+ (1–0) and $H^{13}CO^+$ (1–0) lines are detected for both MM1 and MM2. MM3 has a weak emission in HCO^+ (1–0). As for CS, MM1 emission is stronger and more extended than for MM2 (respective extensions are 104″ × 78″ and 57″ × 56″). With b/a = 0.75 and a position angle of +75°, we note that MM1 emission may be extended along the outflow as expected since the HCO^+ line emission is definitely showing outflow wings such as in CO. The map shows an emission between MM1 to MM2, and MM2 to MM3, confirming that the three sources are connected.

Dense gas traced by H_2CO (3_{22}–2_{21}) line is only detected for MM1 and MM2. The emission from each source coincides perfectly with the dust continuum positions. MM1 and MM2 have similar intensities and have roughly the same small circular size (35″ × 30″, b/a = 0.85 for the two sources) and do not show any spatial suggestions of being contaminated by outflows.

The CO (2–1) line is detected in all sources and shows an extended emission from the whole region. MM1 emission is extended to the west (72″ × 51″, b/a = 0.71 and PA = +85°) due to the red wing of the outflow (PA = +88°). See the following section for more details on the CO outflows.

3.2. Molecular outflows in CO (2–1)

The CO (2–1) line emission shows clear outflow wings. They are due to the already known CO outflow driven by MM1 (Beuther et al. 2002c) but also seem to be located in the region of MM2. Figure 3 displays the average CO (2–1) spectra around MM1 and MM2, as well as the contour map of the integrated emission in the wings. The displayed spectra clearly show emission wings up to high velocities. The observed maximum velocities are −20.4 and +20.6 km s^{-1} for MM1 and −19.7 and +28.3 km s^{-1} for MM2, with respect to v_{LSR} (see Fig. 3 and Table 4). It is clear from the map of this wing emission that there are actually two outflows driven by the two respective cores. The MM2 outflow is actually newly discovered (see Sect. 5.1 for a discussion).

The MM1 outflow appears oriented mostly east-west. This is not quite the orientation observed for the main jet-outflow system recently discussed by Davis et al. (2004) with a NW-SE direction for the H_2 jet (see their Fig. 2). A second H_2 jet, west of MM1 and probably driven by an embedded source in MM1-SW (see Fig. 1), is however also recognized in this work. The position of MM1-SW is marked in Fig. 3 with a small green triangle. Its location is close to a possible secondary center of outflow with a weak blue-shifted lobe in the south and the bright redshifted western lobe being curved toward that location. The spatial resolution of our CO observation is not high enough to fully conclude about the association of CO outflowing gas with the different driving sources, but it seems that the western part of the MM1 outflow might actually be dominated by a second outflow from MM1-SW. The inclination of the MM1 flow on the sky is difficult to determine. From the significant extension of the flow and from the overlap of the lobes, we can only say that

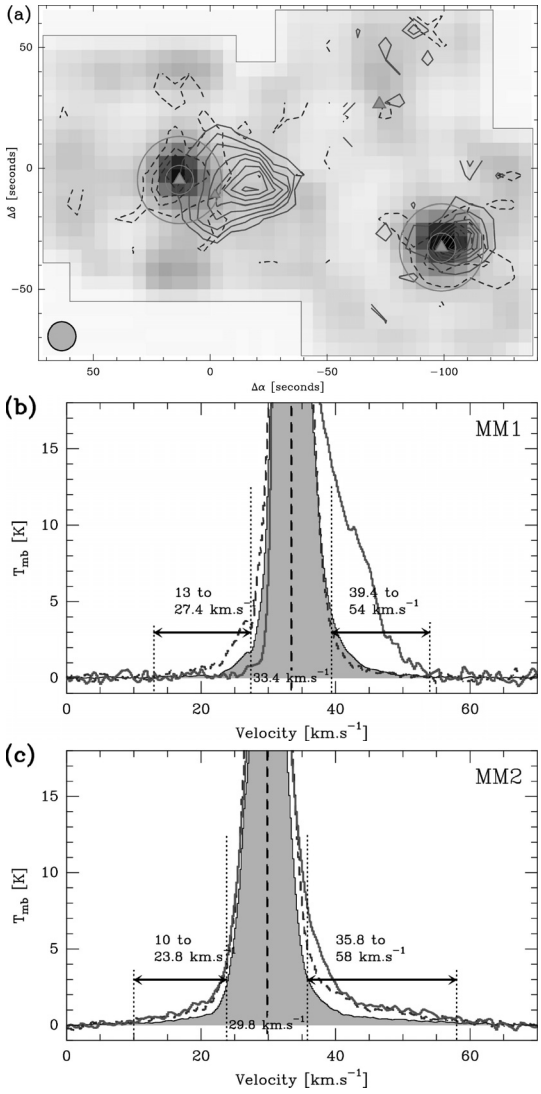

Fig. 3. **a)** Contour maps of the CO (2–1) blue-shifted (dashed) and red-shifted (solid) integrated emission in the outflow wings for MM1, MM2, and MM3 (no detection). Positions of the MM cores are marked by filled (green) triangles. Blue- and red-shifted velocity intervals are +13.0 to +27.4 and +39.4 to +54.0 km s^{-1} for MM1, +10.0 to +23.8 and +35.8 to +58.0 km s^{-1} for MM2 and MM3. Lowest, highest contours and contour steps are (10, 70, 15) K km s^{-1} (blue) and (60, 410, 50) K km s^{-1} (red) for MM1, and (10, 70, 15) K km s^{-1} (blue) and (20, 195, 25) K km s^{-1} (red) for MM2 and MM3. The background grey-scaled image is the integrated H_2CO emission from Fig. 2. **b)** CO (2–1) spectra for the MM1 outflow, together with the velocity cuts used to integrate maps (dotted vertical lines) in **a)** and to derive the mechanical forces. The solid line circles around MM1 and MM2 are 6″and 12″ radius and indicate the area on which the F_{CO} measurements are derived (see text for details). The filled grey spectrum is an average over the region of bright intensities in the wings as seen in the integrated map in **a)**. The dashed and blue (respectively solid and red) spectrum shows the line profile at the maximum of the blue (resp. red) lobe. **c)** Same as **b)** for MM2.

the flow is neither face-on (in the plane of the sky) nor pole-on, and is therefore mostly intermediate.

The MM2 outflow is more compact than for MM1. Both lobes are confined in the core. The integrated emissions in the two lobes are similar in strength and four times stronger than the blue lobe of MM1. If the flow is dominated by a single ejection,

Table 4. Momentum flux of CO (2–1) calculated as in Bontemps et al. (1996).

	Δv_b [km s^{-1}]	Δv_r [km s^{-1}]	F_{CO_b} [$M_\odot$ km s^{-1} yr^{-1}]	F_{CO_r} [$M_\odot$ km s^{-1} yr^{-1}]	$F_{CO_{total}}$ [$M_\odot$ km s^{-1} yr^{-1}]	Ext. blue	Ext. red
MM1	(13.0,27.4)	(39.4,54.0)	$0.44 \pm 0.12 \times 10^{-3}$	$1.86 \pm 0.11 \times 10^{-3}$	$2.30 \pm 0.23 \times 10^{-4}$	$17'' \times 11''$	$46'' \times 45''$
MM2	(10.0,23.8)	(35.8,58.0)	$0.48 \pm 0.09 \times 10^{-3}$	$1.86 \pm 0.15 \times 10^{-3}$	$2.34 \pm 0.24 \times 10^{-4}$	$40'' \times 25''$	$26'' \times 22''$

the large overlap of the two lobes suggests that the flow is not face-on, but could be close to pole-on.

All the derived properties of the two outflows are summarized in Table 4. In addition, to quantify the energetics of the two detected outflows, we derive and give the outflow forces in this table using the procedure described in Bontemps et al. (1996). The mechanical force (or momentum flux) seems to be the measurable quantity from observed CO outflows that can approach in an almost certain way the corresponding quantity of the inner jet or wind (Cabrit & Bertout 1992; Chernin & Masson 1995). We estimated the outflow force F_{CO} for MM1 and MM2 by integrating the momentum flux inside volumes with radius 6″ and 18″ centered on the sources. In addition, for the extended red lobe of MM1, a measurement is given between 18″ and 30″ to cover the red lobe better. Since the inclination of the two outflows cannot be reliably derived from such low-resolution observations, we adopted the average correction of a factor of 10 adopted by Bontemps et al. (1996).

3.3. Raster maps in CS, $C^{34}S$, and H_2CO (3_{12}–2_{11})

In addition to the large maps, a complementary investigation of the three millimeter sources is provided by the 3 × 3 raster maps of CS, $C^{34}S$ and H_2CO (see Fig. 4).

All transitions are detected toward MM1 at $v_{LSR} = 33.4 \pm 0.1$ km s^{-1}. The line profiles are similar with a typical line width (FHWM) $\Delta v = 2.7 \pm 0.2$ km s^{-1}. CS (2–1), CS (3–2), and CS (5–4) have roughly equal intensities. The optically thin $C^{34}S$ (2–1) line emission is detected all around the source at an approximately constant intensity level of ∼1 K. In contrast, $C^{34}S$ (3–2) seems to peak on the central position. The line profiles and the spatial patterns for H_2CO (3_{12}–2_{11}) and CS (5–4) are very similar, suggestive of common origin and excitation conditions for the two transitions (E_{up}/k are equal to 33.40 and 35.27 K).

The intensities of most transitions toward MM2 are weaker than MM1. The line profiles at $v_{LSR} = 29.8 \pm 0.1$ km s^{-1} have a triangular shape and a larger line width ($\Delta v = 3.7 \pm 0.1$ km s^{-1}) compared to MM1. This could be due to a gas motion contribution through its turbulence. The intensity of CS (5–4) is low compared to MM1, contrary to H_2CO (3_{12}–2_{11}) line emission, which is as bright as in MM1.

All molecular line profiles are weaker in MM3, and seem to be less peaked than in MM1 and MM2, as seen in velocity integrated maps (cf. Fig. 2). They are detected at all positions in CS (2–1), (3–2), they have a weak emission in two positions in H_2CO (3_{12}–2_{11}), and finally CS (5–4) and the $C^{34}S$ transitions could not be detected.

3.4. Continuum fluxes

To derive the spectral energy distribution of the three millimeter peaks in IRAS 18151–1208, we retrieved continuum data from the literature. MM1 was imaged for the first time at 450,

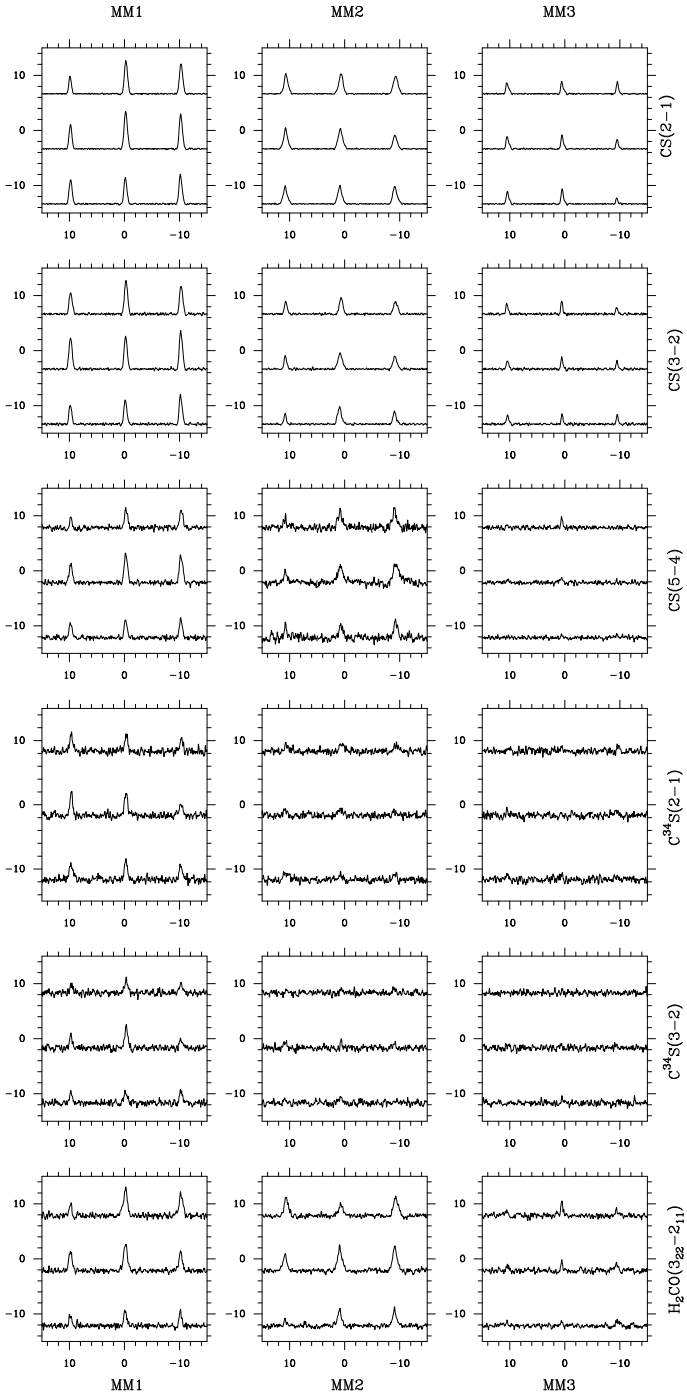

Fig. 4. 3 × 3 maps in CS, $C^{34}S$, and H_2CO (3_{12}–2_{11}) for MM1, MM2, and MM3 sources. Velocity ranges from 15 to 50 km s^{-1} in all spectra, intensity ranges from –2 to 5 K for H_2CO line emission, –1 to 2 K for $C^{34}S$ line emissions, –2 to 5 K for CS (5–4) line emission and –2 to 10 K for other CS line emission. Spectra have been smoothed to an identical velocity resolution of 0.2 km s^{-1}.

Table 5. Continuum flux densities of the three cores within IRAS 18151–1208 region.

	MSX flux densities [Jy]				IRAS flux densities [Jy]				mm-continuum flux densities [Jy]				mm	source
λ [μm]	8.28	12.13	14.65	21.3	12	25	60	100	450	800	1100	1250	size [″]	size [″]
MM1	10.3	21.8	33.0	61.8	19.0	98.6	<891	<1890	49.4	7.62	1.40	1.66	21.3	18.2
MM2	<0.05	<0.21	<0.34	<0.73	<0.38	<1.36	<891	<1890	–	–	–	0.670	18.1	14.4
MM3	<0.07	<0.26	<0.41	<0.82	<0.61	<2.21	<891	<1890	–	–	–	0.261	18.0	14.2

800, and 1100 μm by McCutcheon et al. (1995), then at 450 and 850 μm by Williams et al. (2004), and the overall region at 1.2 mm by Beuther et al. (2002b). Uncertainties are homogenized to account for typical calibration errors taken as 20% in the millimeter range (1.1 and 1.2 mm) and 30% in the submillimeter range (450 and 800 μm). To compare observations and model, we chose the deconvolved dust emission size θ_r as a reference for the SED. We deconvolve using $\theta_\mathrm{r} = \sqrt{\theta_\mathrm{s}^2 - \theta_\mathrm{mb}^2}$, where θ_s is the observed mm-continuum half-peak size derived by Beuther et al. (2002b) and θ_mb the HPBW (11″), using a 2D Gaussian fit, assuming that the source is smaller than the beam and has a Gaussian shape. All millimeter ($\lambda > 450$ μm) peaks S_λ^peak are then adapted to this reference size using

$$S_\lambda = \left(\frac{\theta_\mathrm{r}}{\theta_\mathrm{mb}}\right)^{3+p} S_\lambda^\mathrm{peak} \quad (1)$$

where p is the density power-law index (derived by Beuther et al. 2002b) and S_λ the adapted flux density used to build the SED. These flux densities are 49.4, 7.62, 1.40, and 1.66 Jy at 450, 850, 1100, 1250 μm for MM1, respectively. The process is iterated on MM2 and MM3 and reference sizes with millimeter-continuum peak fluxes are reported in Table 5. Unfortunately, the sub-millimeter continuum data for MM2 and MM3 are less abundant than for MM1 as these two sources were not observed by McCutcheon et al. (1995) and Williams et al. (2004).

Concerning mid- and far-infrared flux density measurements, MSX only detected MM1. Thus we derive a 3σ noise level inside the beam size around the millimeter-continuum position of MM2 and MM3, taken as an upper limit. We note that the IRAS emission of the region is dominated by MM1, which is confusing upper limits for MM2 and MM3. We therefore improved the IRAS map using the publicly available HiRes maximum correlation method (Aumann et al. 1990), showing MM1 detection at 12 μm and 25 μm. At 60 μm and 100 μm, a single peak is detected slightly shifted to the west. We conclude that the huge beam width of IRAS sums the three flux densities from the three sources and the environmental filament contribution. Measured flux densities reported in the IRAS catalog at 60 μm and 100 μm are taken as upper limits for the three sources. All results are shown in Table 5.

4. Modeling the continuum and the molecular emission of MM1 and MM2

In this section we explain how we derive physical models for MM1 and MM2 and how we use them to investigate the kinematics and the molecular abundances inside the cores. Following the method initiated and validated by van der Tak et al. (1999, 2000b), we use the dust continuum emission to derive the density and temperature profiles of the cores. Dust emission is sensitive to the total column density of dust (optically thin part of the SED in the millimeter wave range), and to the dust temperature and its distribution(mid to far-IR range). We try to build the simplest model in order to have the most general representation of the object. Then from the obtained physical model, we can run molecular line modeling to constrain kinematics (line profiles) and chemistry (abundances of observed species). Since MM3 is weak or not detected in a number of molecules and does not have a well-constrained SED, we do not attempt to model it. We instead restrict ourself to a simple discussion of its evolutionary stage.

4.1. IRAS 18151–1208 MM1

4.1.1. Spectral energy distribution

The MM1 core is massive ($M \approx 550\ M_\odot$ according to Beuther et al. 2002b, , applying the correction of 1/2 from the associated 2005 erratum). It coincides with the bright IRAS 18151–1208 source ($L \approx 2.0 \times 10^4\ L_\odot$). In a first approximation, assuming that the object has a spherical symmetry, we want to derive the best radial distribution of density and temperature that can fit the SED and that takes observational constraints into account.

(1) 1D modeling

We used the radiative transfer code MC3D in its 1D version (Wolf et al. 1999) to calculate the expected dust emission. This code is Monte-Carlo based and uses the standard MRN (Mathis et al. 1977) dust grain distribution with the dust opacities from Ossenkopf & Henning (1994). The model parameters are the central stellar luminosity L_*, its temperature T_*, the internal and external radii r_0 and r_ext of the object, the molecular hydrogen density n_0 at r_0, and the power-law index p of the density distribution in the form $n(r) = n_0(r/r_0)^p$.

The bolometric luminosity is derived by integrating the SED, and we obtain $L_\mathrm{bol} = 1.4 \times 10^4\ L_\odot$. The temperature of the central star is taken as the corresponding main sequence star, i.e. $T_* = 22\,500$ K (type B2V of 10 $M_\odot$ approximatively, cf. Underhill et al. 1979). We adjust r_0 to fit the dust sublimation radius where $T \simeq 1500$ K. The external radius r_ext of the model is derived from the radius of the 1.2 mm continuum emission (here the deconvolved mean of major and minus axes given by Beuther et al. 2002b) assuming that the source has a Gaussian shape smaller than the beam size. The resulting extension is 18.2″, hence $r_\mathrm{ext} = 27\,300$ AU or ≃0.13 pc at 3 kpc. The power-law index p is set to −1.2 according to the continuum profile fit by Beuther et al. (2002b). Finally the only free parameter left is n_0, and it is derived by fitting optically thin 1.2 mm continuum emission with a χ^2 calculation. We find $n_0 = 2.8 \times 10^9$ cm^{-3} at $r_0 = 21$ AU with $\chi^2 = 3.94$, hence $\langle n \rangle = 8.0 \times 10^5$ cm^{-3} and a total mass of gas equal to 660 $M_\odot$. Outer and mean temperatures, formally T_ext and $\langle T \rangle$, are respectively 25.4 K and 27.3 K. The derived temperature profile can be fitted with a power law of the form $\log_{10}(T) = \alpha \log r + \beta$ with $\alpha = -0.588$ and $\beta = 3.95$.

The resulting SED (see Fig. 5) shows that millimeter and sub-millimeter continuum parts are well modeled. In contrast, the mid- and far-infrared emission is not reproduced, due

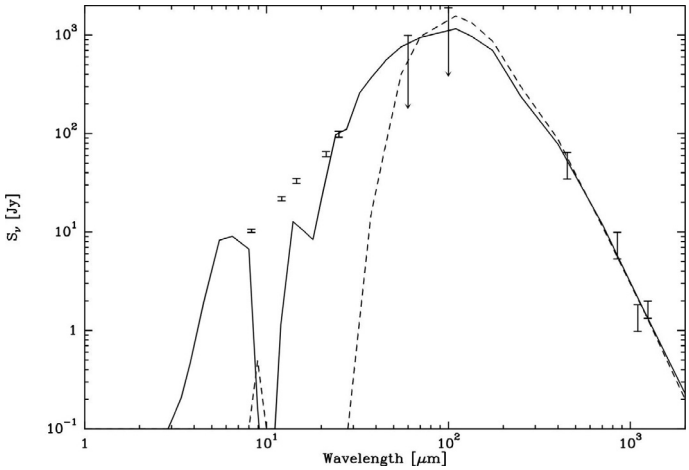

Fig. 5. Spectral energy distributions obtained from 1D (dashed line) and 2D models (continuous line) overlaid on observed fluxes of MM1 source. Dust continuum peak fluxes have been adjusted to fit radial extension of the model. Mid-infrared fluxes are obtained in 2D by choosing a typical view angle $\theta_{\rm los} \sim 45°$ (90° = edge-on view).

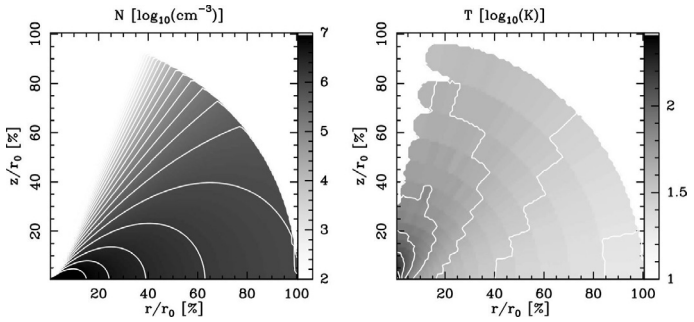

Fig. 6. Density and temperature distributions for the 2D model presented on a logarithmic grey scale, with 20 logarithmic levels from 10^2 to 10^7 cm^{-3} for density and 10 logarithmic levels from 10 K to 263 K.

to spherical symmetry that does not permit infrared photons, coming from inner parts, to leave the source without being reprocessed into photons at millimeter wavelengths. The 2D modeling, where the polar regions contain less matter than in the midplane, should therefore reproduce the observed mid-infrared emission better.

(2) 2D modeling

We used the 2D version of the MC3D code that was developed for disks. It is parametrized in the radial and altitude directions (r, z), and it assumes the Keplerian disk equilibrium by Shakura & Syunyaev (1973):

$$n(r,z) = \begin{cases} n_0 \left(\frac{r}{r_0}\right)^p \mathrm{e}^{-\pi c^2 z^2 \sqrt{2 r_{\rm ext}} r^{-2.5}} & \text{if } r \in [r_0; r_{\rm ext}] \\ 0 & \text{otherwise.} \end{cases} \quad (2)$$

We note that the model has three free parameters: n_0 determined as for the 1D modeling, the inverse height of scale c, and the source angle relative to the line of sight $\theta_{\rm los}$. It is mostly $\theta_{\rm los}$ that controls the fraction of mid-infrared emission. Values close to 45° can reproduce the SED roughly, and we do not adjust the value further to keep the model as general as possible. The inverse height of scale c controls how thin the disk-like structure is. Since MM1 is young and is still mostly a spherical core, we try to keep c as small as possible while always having a significant mid-infrared emission for typical, average lines of sight. Thus c was gradually increased from 0.4 by 0.1 steps until an infrared emission greater than 0.1 Jy (limit of detection in the observations) could be obtained, finally leading to $c = 0.7$. Other parameters are kept identical as in the 1D model (T_*, L_*, r_0, $r_{\rm ext}$, and p). Calculations show that the best fit is obtained for $n_0 = 2.7 \times 10^9$ cm^{-3} with $\chi^2 = 0.732$ (total mass $M = 830\ M_\odot$). The derived SED is plotted in Fig. 5. It illustrates how a 2D modeling can reproduce the observed infrared emission better, although the silicate feature is not matched. We display the resulting density and temperature distributions in Fig. 6. One can see that the equatorial regions are denser and colder than around the polar axis. This is why mid-IR emission can escape and directly contribute to the SED.

4.1.2. CS and C^{34}S line emissions

Since molecular line emission is usually dominated by the mostly spherical external layers of the protostellar cores, the 2D description might not be required to reproduce molecular lines.

We used the CS and C^{34}S line emission to compare the results of modeling in 1D and 2D geometries. We directly used outputs of continuum models described above, assuming that dust and gas temperatures are equal, to which we added parameters for molecular abundances and kinematics. The molecular abundances relative to H_2, X(CS), and X(C^{34}S), mostly determine the line intensities when the opacity is low ($\tau \lesssim 1$). Then we used a constant turbulent velocity $v_{\rm T}$. It is the main contributor to the line width compared to the thermal dispersion. Both X(CS) and $v_{\rm T}$ are therefore the free parameters to fit the intensities and widths of the line emission we observed. Finally we want to test whether an infall motion in our model could improve our results, giving at least an upper limit for it. The infall velocity is parameterized by the free-fall, power-law distribution $v_{\rm in}(r) = v_{\rm in}\,(r/r_0)^{-0.5}$ (Shu 1977). We test its effect on modeled line emission by switching between $v_{\rm in} = 0$ and $v_{\rm in} = -0.4$ km s^{-1}, the lowest value that modifies modeled line emission significantly for MM1.

The line profiles are computed with the RATRAN code (Hogerheijde & van der Tak 2000). This code allows 1D and 2D modeling respectively using multi-shell and grid descriptions of the object. The radiative transfer calculation uses the Monte-Carlo method to derive the populations of the energy levels and then builds data cubes that are convolved with corresponding beam sizes of the telescope to be directly compared with the observations.

In the 1D (spherical) geometry, a χ^2 calculation is performed for the optically thin C^{34}S line ($\tau_{2-1} = 9.0 \times 10^{-2}$ and $\tau_{3-2} = 2.2 \times 10^{-1}$) over a grid for $f_{\rm C^{34}S} = X({\rm C^{34}S})/X({\rm C^{34}S})_{\rm typ}$ (with $X({\rm C^{34}S})_{\rm typ} = 1.0 \times 10^{-10}$) and $v_{\rm T}$. The best fit is obtained for $(f_{\rm C^{34}S}, v_{\rm T}) = (0.5, 1.0)$ with $\chi^2 = 0.956$. Then the grid is refined only for $f_{\rm C^{34}S}$, because model results are less dependent on $v_{\rm T}$ (kept equal to 1.0 km s^{-1}). The best result is obtained for $f_{\rm C^{34}S} = 0.51$ with $\chi^2 = 0.952$, leading to the abundance $X({\rm C^{34}S}) = 5.1 \times 10^{-11}$. Assuming a typical [S/^{34}S] isotopic ratio of 20 (Wilson & Rood 1994; Chin et al. 1996; Lucas & Liszt 1998), the CS emission is modeled with the abundance $X({\rm CS}) = 1.0 \times 10^{-9}$.

The final results of the line modeling are displayed in Fig. 7. Given the very small number (2) of free parameters, the resulting fits are quite good. It reproduces the line intensities well. Only the profiles for the higher excitation lines indicate a significant difference between observations and this simple model. There

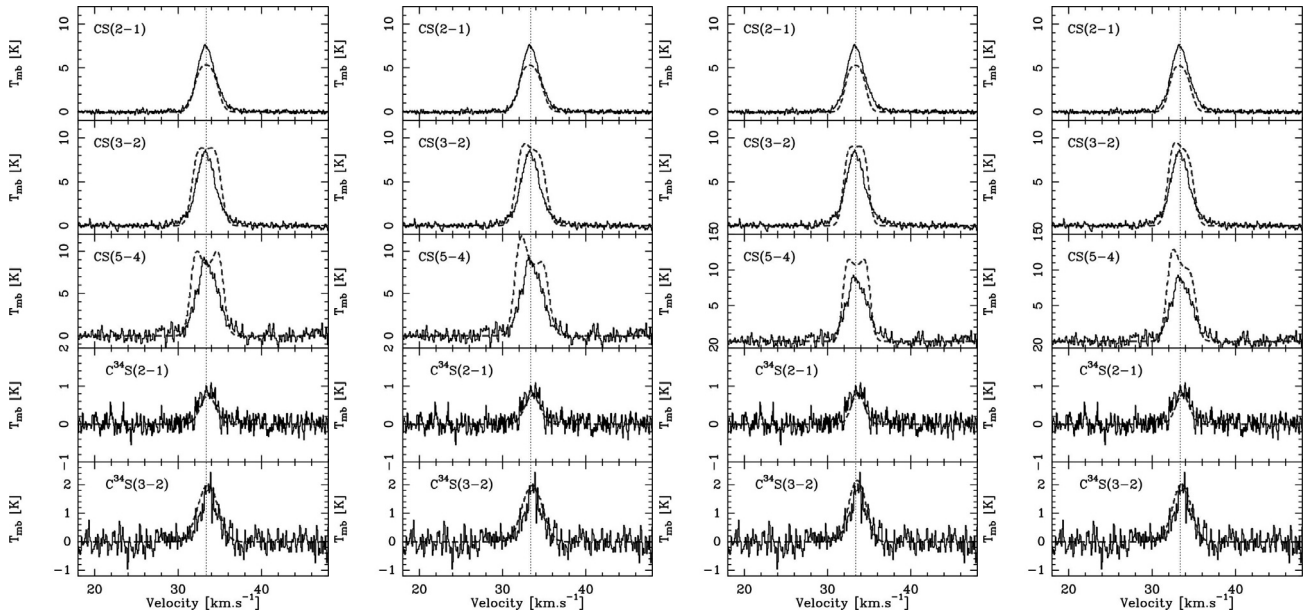

Fig. 7. Emission of CS and $C^{34}S$ from MM1 object (continuous line) overlaid by – from left to right – 1D static, 1D with infall (v_{in} = −0.4 km s^{-1}), 2D static, and 2D with infall (v_{in} = −0.4 km s^{-1}) model line emissions (dashed). Velocity resolutions of spectra are kept identical to the observational resolutions reported in Table 2.

are clear self-absorptions for the (3–2) and the (5–4) transitions (τ_{5-4} = 3.6), which indicate an overestimate of high CS column densities for the highest excitation regions (central regions). This could well be due to a significant decrease in the CS abundance toward to the center of the core (see Sect. 5.5 for a discussion).

We find that a minimum infall velocity of −0.4 km s^{-1} is needed to start to see a clear, asymmetric shape of the profile. Introducing infall improves only slightly the results for the (2–1) and (3–2) transitions and makes the fit of the (5–4) transition worse (cf. Fig. 7, second plot from the left). We conclude that an infall velocity in the 1D model does not improve the fits, and we consider the value of −0.4 km s^{-1}as an upper limit.

For the 2D modeling, the same χ^2 adjustment is performed for v_T and $f_{C^{34}S}$. Interestingly enough, the final best fit is exactly the same as in the 1D geometry with $X(CS) = 1.0 \times 10^{-9}$ and $X(C^{34}S) = 5.1 \times 10^{-11}$. We note that line profiles and relative intensities between the transitions are similar to the 1D case. Only a very slight improvement in the profile of CS (5–4), which is less self-absorbed, can be noted. The result is shown on the third plot from the left in Fig. 7.

Again the effect of an infall velocity on the line profiles is tested. With v_{in} = −0.4 km s^{-1} we note that the asymmetric profile of the line emission is not as strong as in the 1D case (cf. Fig. 7, fourth plot from the left). We however conclude that infall in the 2D case does not critically improve the results.

Comparison between 1D and 2D modeling shows that using a spherical description of the source is sufficient to reproduce CS and $C^{34}S$ molecular line emission, even if 2D is slightly better with less self-absorption than in the 1D case. In addition we conclude that infall motion is not clearly detected and is not necessary to reproduce observations of MM1. We thus decide to use only 1D modeling without infall motion for the other observed lines.

That 2D modeling is not needed for the CS line emission can be explained by the optical depth, which is not high at the corresponding frequencies compared with the mid-IR continuum, or by the asymmetry that is significant only on small scales where the temperature is high (between 300 and 1000 K). The observed molecular lines do not trace these inner regions.

4.1.3. Other lines: N_2H^+, HCO^+, $H^{13}CO^+$, and H_2CO

We adopt the 1D model derived in the previous section. For each molecule, the only free parameter left is therefore its relative abundance to H_2.

(1) N_2H^+ (J = 1–0) modeling

The N_2H^+ (J = 1–0) is split by hyperfine structure. Theoretically there are 15 hyperfine components, which blend into seven for sources with low turbulence (Caselli et al. 1995) or into three if turbulence is strong, as in our case. To fit observations correctly from ATNF telescope at Mopra, we created the molecular datafile for the RATRAN radiative transfer code. Energy levels, Einstein coefficients A_{ul}, and collisional rates γ_{ul} are derived from Daniel et al. (2004) through the BASECOL database maintained by the Observatoire de Paris[5].

Energy levels included in the molecular datafile vary from J = 0 to J = 6. The hyperfine structure resulting from angular momentum and nuclear spin interaction (F_1 and F quantum numbers) leads to a total of 55 energy levels. The statistical weight $n_{J,F_1,F}$ of each level is simply determined by the good quantum number F (see Daniel et al. 2005):

$$n_{J,F_1,F} = 2F + 1 \quad (3)$$

The molecular data file takes 119 radiative transitions into account where the first 15 of them fit to the (J = 1–0) transition. The spectra obtained are then summed to finally reproduce the whole composite profile of the triplet (see Fig. 8).

Collision rates γ_{ul} reported by Daniel et al. (2004) are given for helium as the collision partner. As described by Schöier et al. (2005), we take 1.4 × γ_{ul} to correct for an H_2 collision partner. Initially collision rates are given for temperatures from 5 K to 50 K, which is the temperature range of the outer parts of our

[5] http://amdpo.obspm.fr/basecol/

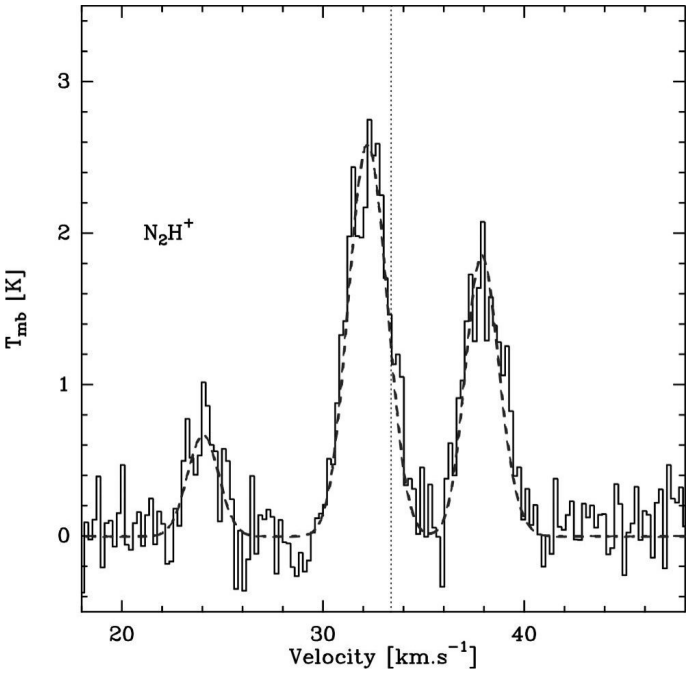

Fig. 8. Emission of N_2H^+ from MM1 object overlaid by 1D model of the source (dashed line). The triplet shape is completely reproduced using our RATRAN molecular datafile. Velocity resolutions of spectra are kept identical to the observational resolutions reported in Table 2.

sources. To be able to model the entire sources, we extrapolated the rates to high temperatures using a least-squares method that derives collisional rates from a linear fit of the form

$$\log(\gamma_{ul}) = a.\log(T) + b. \quad (4)$$

This extrapolation has the advantage of fitting the global trend of the collisional rate without any exaggerated values for high temperatures.

Emission of N_2H^+ is considered as optically thin ($\tau \sim 10^{-2}$) due to its typically low abundance. Thus we model it by comparing the velocity integrated fluxes of observation and model starting from a typical abundance $X(N_2H^+) = 1.0 \times 10^{-11}$. The ratio of modeled to observed fluxes is then used to further correct the abundance while verifying that the line profile is always correctly reproduced. Iterating the process gives $X(N_2H^+) = 3.5 \times 10^{-10}$. An overlay of the model on the observation is shown in Fig. 8.

(2) HCO^+ and $H^{13}CO^+$ (J = 1–0) modeling

The HCO^+ and $H^{13}CO^+$ lines are good tracers of high-density gas and of its kinematics. The $H^{13}CO^+$ (J = 1–0) emission is usually optically thin (here we finally get $\tau = 3.4 \times 10^{-2}$) so we adopt the same routine to derive molecular abundances as for N_2H^+. We then get an abundance of $X(H^{13}CO^+) = 3.4 \times 10^{-11}$. When applying a typical isotopic ratio $[^{12}C]/[^{13}C] = 67$ (Wilson & Rood 1994; Lucas & Liszt 1998), we modeled the HCO^+ line with $X(HCO^+) = 2.3 \times 10^{-9}$. Results are shown in Fig. 9. The resulting modeled HCO^+ line is optically thick (τ = 1.7), reaching a maximum intensity of ~4 K. It suggests that the region of emission in the model is smaller than the telescope beam as expected for a high-density tracer. On the other hand, the observed intensity and profile are very different. It indicates that the bulk of the HCO^+-rich gas does not follow the general distribution of matter indicated by other tracers (dust emission and optically thin lines). The HCO^+ (J = 1–0) line seems to have

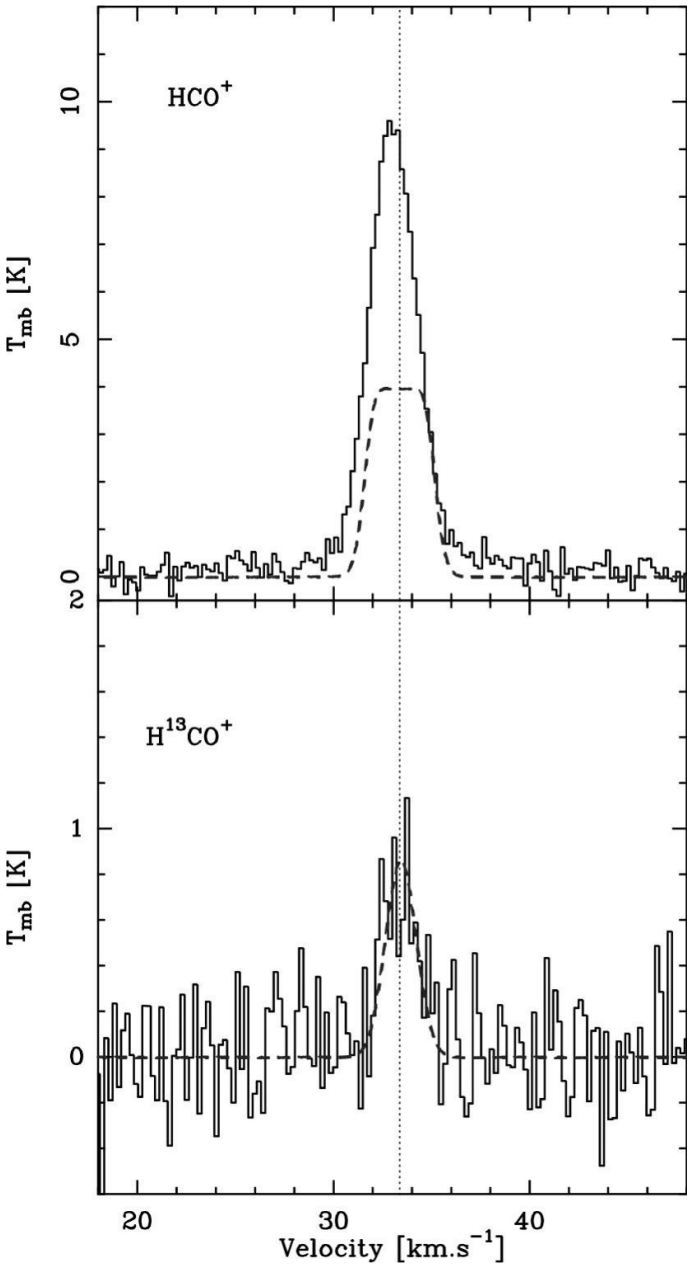

Fig. 9. Emission of HCO^+ (*top*) and $H^{13}CO^+$ (*bottom*) (J = 1–0) from MM1 source overlaid by 1D model of the source (dashed line). Resulting abundances are $X(HCO^+) = 2.3 \times 10^{-9}$ and $X(H^{13}CO^+) = 3.4 \times 10^{-11}$, according to the typical isotopic ratio $[^{12}C]/[^{13}C] = 67$. Velocity resolutions of spectra are kept identical to the observational resolutions reported in Table 2.

an excess on the blue side, which could be associated with the blue-shifted outflow wing that is mostly located inside the core in CO (see Fig. 3). Generally speaking, HCO^+ is a good outflow tracer, and we speculate that the HCO^+ line is actually dominated by some HCO^+-rich gas associated with the outflow shocks inside the core (i.e. at high density as required to excite HCO^+). This would mean that the derived HCO^+ abundance in the core envelope is only an upper limit and could well be much smaller, except locally in outflow shocks.

(3) para- and ortho-H_2CO modeling

The ratio between para and ortho populations of H_2CO is an interesting parameter in the global context of gas temperature

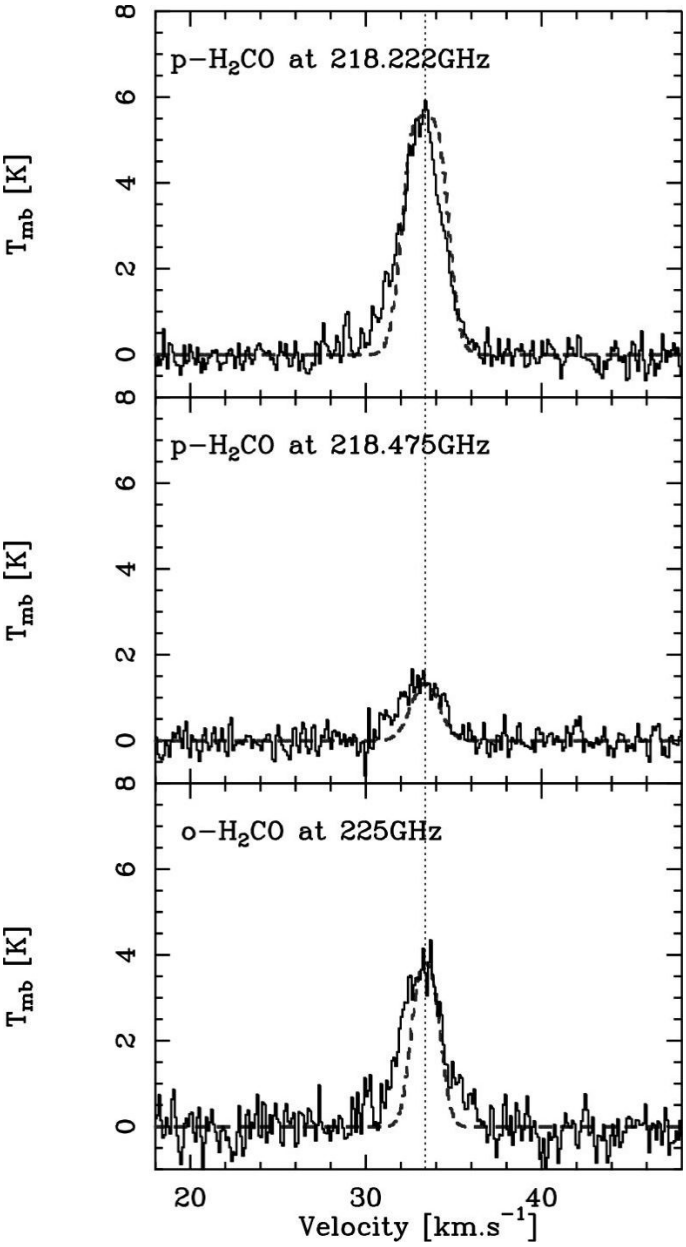

Fig. 10. Para-H_2CO (*top and middle*) and ortho-H_2CO (*bottom*) emissions from MM1 source overlaid by 1D model of the source (dashed lines). Resulting abundances are $X(\text{para}-H_2CO) = 1.5 \times 10^{-10}$ and $X(\text{ortho}-H_2CO) = 1.3 \times 10^{-10}$, leading to a ratio para/ortho ≃1.2. Velocity resolutions of spectra are kept identical to the observational resolutions reported in Table 2.

and chemical activity (Kahane et al. 1984) and can be a useful tool for following the chemical evolution of gas inside and between the observed sources. Our modeling indicates that the lines are mostly optically thin ($\tau_{218.2\text{GHz}} = 1.37$, $\tau_{218.5\text{ GHz}} = 0.09$ and $\tau_{225\text{ GHz}} = 0.77$), so we adopt the same routine as described for N_2H^+. The abundances obtained are as follows $X(\text{para}-H_2CO) = 1.5 \times 10^{-10}$ and $X(\text{ortho}-H_2CO) = 1.3 \times 10^{-10}$, leading to a ratio para/ortho ≃1.2. The agreement between the modeled and the observed lines is good. All the lines, however, tend to show some excess on the blue side, while the ortho line even shows excesses on both sides (see Fig. 10). In addition we want to emphasize that the two para-H_2CO transitions, which have two significantly different E_{up}/k (respectively 21.0 K and 68.1 K), are well-reproduced. This is an indication

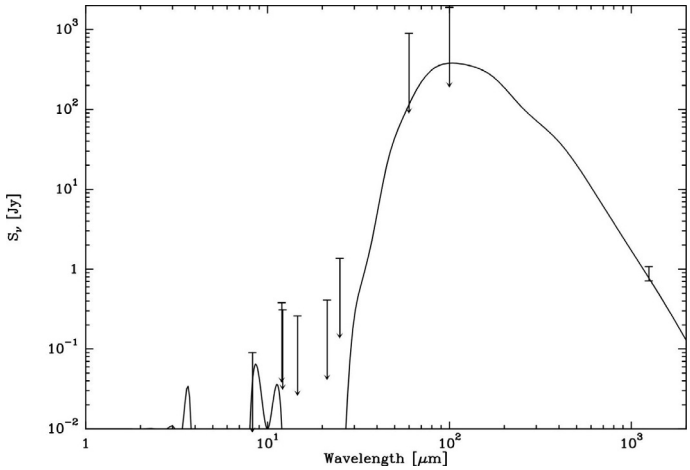

Fig. 11. Spectral energy distribution of MM2 overlaid with the 1D model result. Infrared emission always has an upper limit due to the non-detection of the source.

that the excitation temperature of the emitting gas is also well-reproduced by the physical model.

4.2. IRAS 18151–1208 MM2

4.2.1. Spectral energy distribution

Since MM2 is not detected in the mid-infrared and considering our conclusions from the modeling of MM1, we decided to only model the source in a simple 1D, spherical geometry. We cannot derive the bolometric luminosity of MM2 by integrating its SED, due to all infrared fluxes being upper limits. Instead, we assumed a luminosity of 2700 $L_\odot$, which is uncertain by at least a factor of 2. This luminosity corresponds to a B4V type star (approximatively 7 $M_\odot$) with $T_* = 16\,600$ K, which we used to describe the heating source of our model. The 1.2 mm continuum source deconvolved extension from Beuther et al. (2002b) is equal to 14.4″, thus $r_{\text{ext}} = 21\,600$ AU or ≃0.10 pc at 3 kpc, and we assume a power-law index $p = -1.3$ from the same paper. Because only one mm-wave peak flux density was measured for MM2 (see Table 5), we adapted n_0 to fit this unique measurement. After two iterations we converged to $n_0 = 1.1 \times 10^{10}$ cm^{-3} at $r_0 = 12.4$ AU, hence $\langle n \rangle = 1.1 \times 10^6$ cm^{-3} and a total mass gas of $M = 460\ M_\odot$. We derived $T_{\text{ext}} = 19.2$ K, $\langle T \rangle = 19.4$ K and the temperature could be fitted by a power law of the form $\log_{10}(T) = \alpha . \log r + \beta$ with $\alpha = -0.614$ and $\beta = 3.85$. The resulting SED does not show any emission in the mid- and far-infrared, in agreement with the observations (see Fig. 11) and as expected for a simple 1D description.

4.2.2. Molecular emission modeling

We used the same procedure to model the molecular lines toward MM2 as for MM1. We therefore derived the molecular abundance relative to H_2 and the turbulent velocity v_T. We also tested a possible infall velocity field in the form $v_{\text{in}}(r) = v_{\text{in}}\,(r/r_0)^{-0.5}$.

Emission of optically thin $C^{34}S$ lines ($\tau_{2-1} = 4.4 \times 10^{-2}$ and $\tau_{3-2} = 4.4 \times 10^{-2}$) in the MM2 object are treated by taking two different grids for the χ^2 calculation over its intensity and area. The first grid is $(f_{C^{34}S}, v_T) = ([0.1, 0.2 \ldots 0.5], [1.5, 1.6 \ldots 2.0])$, and it shows a best fit for $(f, v_T) = (0.3, 1.7)$. The second one is finer with $f_{C^{34}S} = [0.25, 0.26 \ldots 0.35]$ and a fixed $v_T = 1.7$ km s^{-1} because of the low dependence of the modeled line on this

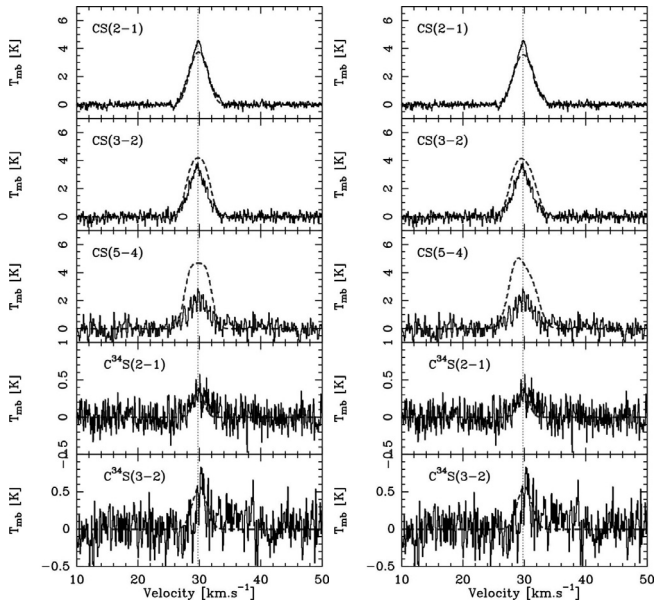

Fig. 12. Emission of CS from MM2 object overlaid by 1D static (*left*) and 1D with the infall ($v_{in} = -1.0$ km s^{-1}) model of the source (dashed lines). Velocity resolutions of spectra are kept identical to the observational resolutions reported in Table 2.

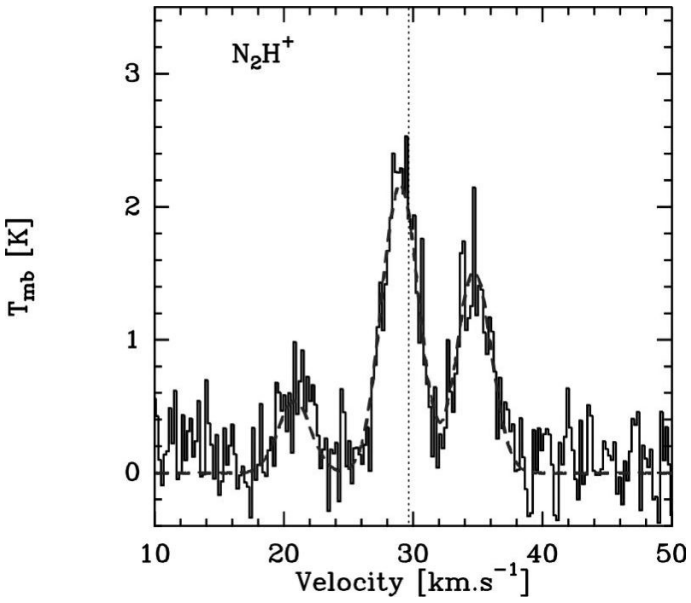

Fig. 13. Line emission of N_2H^+ from MM2 object overlaid by the 1D model of the source (dashed line). Velocity resolutions of spectra are kept identical to the observational resolutions reported in Table 2.

parameter compared to $f_{C^{34}S}$. It gives the best fit for $f_{C^{34}S} = 0.27$, hence an abundance $X(C^{34}S) = 2.7 \times 10^{-11}$. As for MM1, the resulting modeled lines reproduce all transitions well except the CS (5–4) line, which is heavily overestimated in intensity. Again it points to a lower abundance of CS in the inner regions compared to the outside.

Then, as above for MM1, we added an infall velocity profile following a typical $r^{-0.5}$ distribution. The asymmetric shape was obtained for a minimum infall velocity $v_{in} = -1.0$ km s^{-1}. The resulting profile is unchanged for (2–1) transition, is slightly improved for the (3–2), but shows an excess of blue emission that is not observed for CS (5–4) (see Fig. 12, right). Therefore including infall velocity distribution does not improve our fit, so does not seem to be necessary. It gives an upper limit for the infall velocity of $v_{in} = -1.0$ km s^{-1}.

The optically thin emission of N_2H^+ ($\tau \sim 10^{-2}$) in MM2 is treated by comparing the observed and modeled velocity-integrated area and using it to adapt an initial typical abundance (1.0×10^{-10}). The resulting fit for N_2H^+ is shown in Fig. 13 and corresponds to $X(N_2H^+) = 6.3 \times 10^{-10}$. As for MM1, the quality of the fit is high.

For HCO^+ and $H^{13}CO^+$, we obtain the following abundances: $X(HCO^+) = 5.1 \times 10^{-9}$ and $X(H^{13}CO^+) = 7.6 \times 10^{-11}$. The best-fit result is shown in Fig. 14. As for MM1, the modeled HCO^+ line emission does not reproduce the observations well. The HCO^+ column density derived from the $H^{13}CO^+$ line implies a heavily saturated ($\tau = 19$) HCO^+ line that is not observed. Obviously in contrast to all the other molecules, the distribution of HCO^+ does not follow the simple spherical geometry of the model.

We then derived the best abundances for the para and ortho-H_2CO to reproduce the three observed transitions (see Fig. 15). The abundance obtained for the ortho transition at 225 GHz is $X(\text{ortho} - H_2CO) = 2.0 \times 10^{-10}$. For the two para transitions, no unique abundance can be derived. For the best fit of the 218.222 GHz line emission, the abundance obtained is $X(\text{para} - H_2CO) = 2.6 \times 10^{-10}$, but the 218.475 GHz line is then too weak by a factor of almost 2; see Fig. 15. At the other extreme, if the 218.475 GHz line is fitted, the abundance obtained is $X(\text{para} - H_2CO) = 4.8 \times 10^{-10}$. In contrast to MM1 for which a correct ratio of the two para lines was obtained, the modeled ratio (218.222 over 218.475) for MM2 appears to be too high. That the weaker 218.475 GHz line emission has a higher upper energy level ($E_{up}/k = 68.1$ K) suggests that the emitting gas is actually warmer in MM2 than what is represented by the simple 1D model. The resulting para-to-ortho ratio is therefore in the range ≃1.3– 2.4.

5. Discussion

5.1. MM2: a new massive protostar driving a powerful outflow.

MM2 is a millimeter source without an infrared counterpart (MSX or IRAS). It is even seen in absorption over the local background in the MSX 8μm image (see Fig. 1). A water maser has been detected toward the core by Beuther et al. (2002a). With the addition of our newly discovered CO outflow driven by MM2, it all clearly points to the protostellar nature of MM2. Inside the core size of 0.22 pc (14.4″, see Table 5), a total mass of 460 $M_\odot$ is obtained with MC3D (dust emissivity for the MRN grain distribution; see Table 6). MM2 is therefore a newly discovered massive protostellar core that is not detected in the mid- or far-IR: an IR-quiet massive protostellar object. A more complete comparison with the detailed analysis obtained for low-mass protostars and in Cygnus X by Motte et al. (2007) is given in the next section.

5.2. Evolutionary stages of MM1, MM2 and MM3.

In contrast to low-mass star formation (e.g. André et al. 2000), the evolutionary sequence for high-mass stars is not well-constrained and understood. The general lack of spatial resolution leads to discussions of evolutionary sequences mostly applied to massive clumps (such as HMPOs, typical size of 0.5 pc) or to high-mass dense cores (typical size of 0.1 pc),

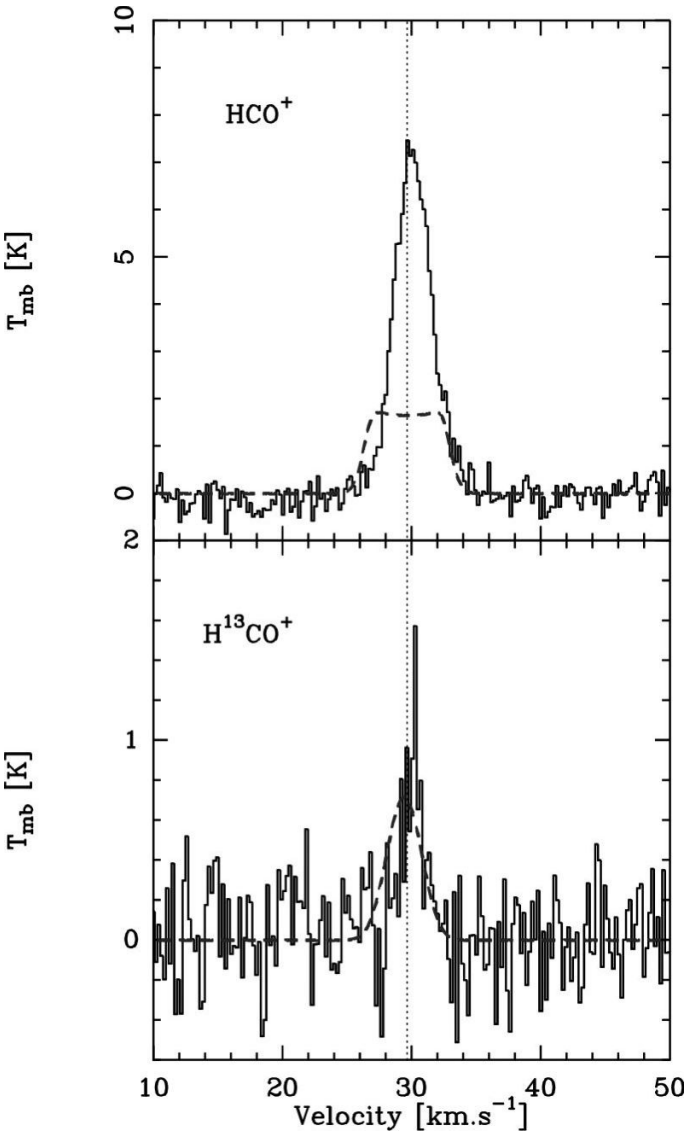

Fig. 14. Emissions of HCO^+ (*top*) and $H^{13}CO^+$ (*bottom*) (J = 1–0) from MM2 source overlaid by 1D model of the source (dashed line). Velocity resolutions of spectra are kept identical to the observational resolutions reported in Table 2.

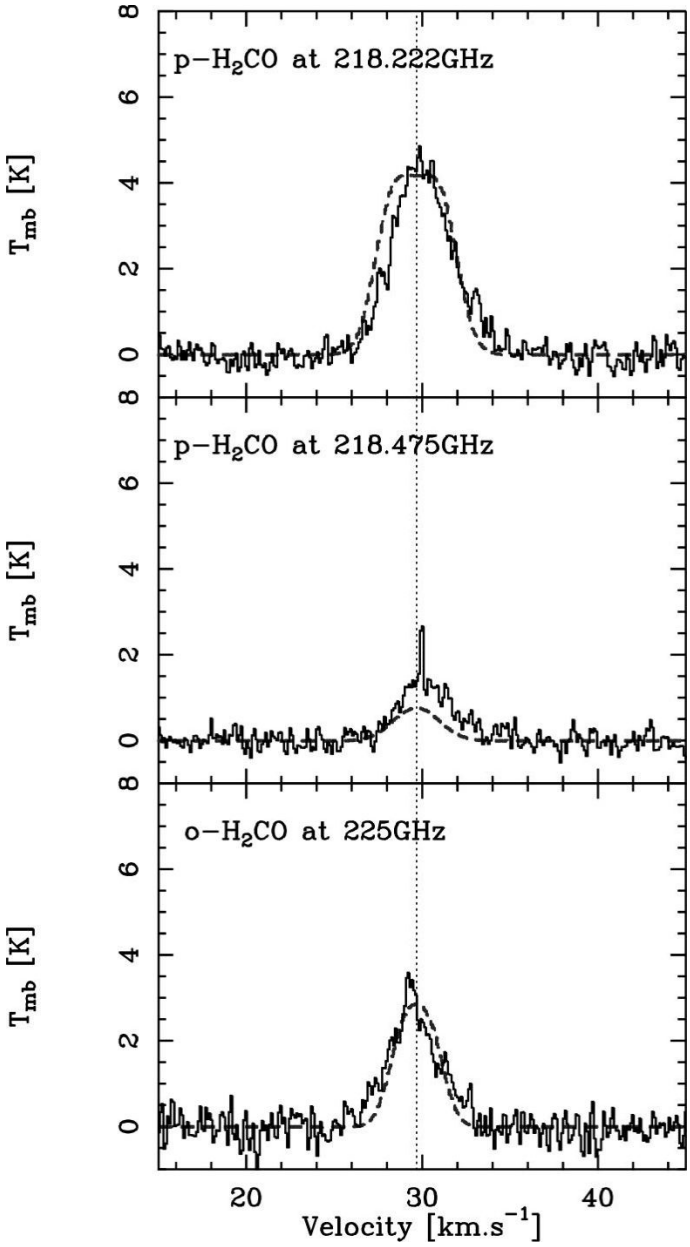

Fig. 15. Para-H_2CO (*top and center*) and ortho-H_2CO (*bottom*) emissions from MM2 source overlaid by 1D model of the source (dashed lines). Velocity resolutions of spectra are kept identical to the observational resolutions reported in Table 2.

which cannot usually be directly compared to protostars that have physical sizes close to 0.01–0.05 pc (e.g. Motte et al. 1998; Motte & André 2001). A recent attempt to clarify these different scales and associated evolutionary sequences is compiled in Motte et al. (2007); see their Table 4. From the complete survey of the relatively nearby Cygnus X complex, a total of 40 high-mass dense cores were recognized with an average size of 0.13 pc, similar to the sizes of nearby, low-mass dense cores, but 20 times more massive and 5 times denser. These high-density cores were all found to already be protostellar in nature and were proposed to represent the earliest phases of high-mass star formation. Among the 40 cores, 15 were already associated with a UC-HII region and bright in the infrared, 8 were only bright in the infrared, and 17 were IR-quiet protostellar cores. This sequence is supposedly to be mostly an evolutionary sequence, the IR-quiet cores being the precursors of the IR-bright cores and then of UC-HII regions. We discuss the cores in IRAS 18151–1208 in the framework of these recent Cygnus X results.

First of all, no bright radio source is detected in the whole IRAS 18151–1208 clump. All the massive protostellar objects detected in the clump are necessarily objects in an evolutionary stage prior to the formation of a UC-HII region. In Fig. 1, the distribution of mid-infrared emission from MSX is displayed. It is clear that the main bright infrared source is associated with MM1, while the MM2 area is devoid of mid-infrared emission. The core is even actually seen in absorption over the local background. MM3 is more complicated since a moderately bright MSX source is situated close to the center of the core.

MM1 has a mass of 660 $M_\odot$ in a radius of 27 300 AU (core size of 0.27 pc) obtained from the fit of the SED with MC3D (Table 6). It has a bolometric luminosity higher than 10^4 $L_\odot$, and is bright in the mid-IR ($S_{20\mu m}$ = 61 Jy). It drives a powerful bipolar outflow and therefore hosts at least one mid-IR bright massive

Table 6. Summary of results from dust continuum emission modeling (above mid-line) and from molecular line emission modeling (below mid-line). The relative uncertainties are at the 3σ level, and they correspond to the rms noise propagated through the modeling process.

	MM1	MM2
L	14 000 $L_\odot$	2 700 $L_\odot$
T_*	22 500 K	16 600 K
$M_{\rm gas}$	660 ± 130 $M_\odot$	460 ± 100 $M_\odot$
$r_{\rm ext}$	27 300 AU	21 600 AU
n_0	$2.8\,(0.6) \times 10^9$ cm^{-3}	$1.1\,(0.2) \times 10^{10}$ cm^{-3}
$\langle n \rangle$	$8.0\,(2.0) \times 10^5$ cm^{-3}	$1.1\,(0.2) \times 10^6$ cm^{-3}
p	−1.2 [a]	−1.3 [a]
$T_{\rm ext}$	25.4 (0.5) K	19.2 (0.4) K
$\langle T \rangle$	27.3 (0.2) K	19.4 (0.2) K
α	−0.588 (0.011)	−0.614 (0.012)
β	3.95 (0.03)	3.85 (0.04)
$r_{\rm in}$	21 (2) AU	12 (1) AU
$v_{\rm T}$	1.0 (0.1) km s^{-1}	1.7 (0.1) km s^{-1}
X(CS)	$1.0\,(0.3) \times 10^{-9}$	$5.4\,(1.5) \times 10^{-10}$
X(C^{34}S)	$5.1\,(1.4) \times 10^{-11}$	$2.7\,(0.8) \times 10^{-11}$
X(N_2H^+)	$3.5\,(0.8) \times 10^{-10}$	$6.3\,(1.4) \times 10^{-10}$
X(HCO^+)	$2.3\,(0.7) \times 10^{-9}$	$5.1\,(1.6) \times 10^{-9}$
X($H^{13}CO^+$)	$3.4\,(1.1) \times 10^{-11}$	$7.6\,(2.4) \times 10^{-11}$
X(p-H_2CO)	$1.5\,(0.4) \times 10^{-10}$	$2.6\,(0.7)$–$4.8(1.3) \times 10^{-10}$
X(o-H_2CO)	$1.3\,(0.4) \times 10^{-10}$	$2.0\,(0.6) \times 10^{-10}$
[para/ortho]	≃1.2	≃1.3–2.4

[a] Values from continuum map analysis by Beuther et al. (2002b).

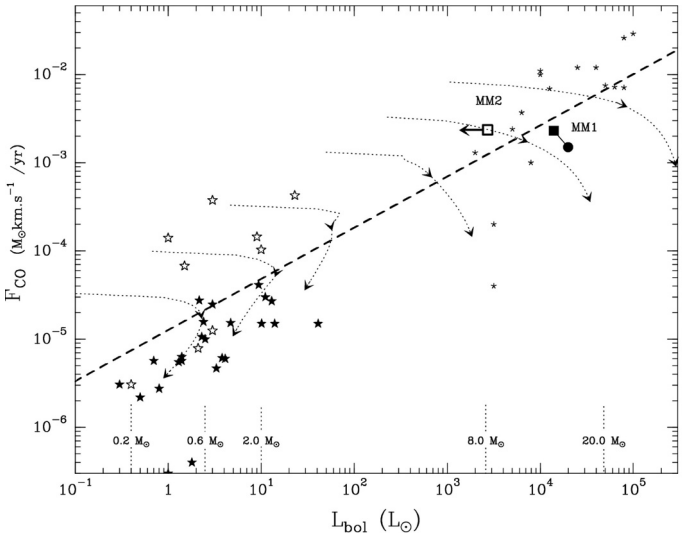

Fig. 16. Diagram of the bolometric luminosities versus CO outflow momentum fluxes for protostars adapted from Fig. 5 in Bontemps et al. (1996). Big starred markers (black and white): low-mass protostars (Bontemps et al. 1996); small starred markers: unresolved massive protostars in HMPOs from Beuther et al. (2002c). The dotted tracks arrows are from the Bontemps et al. (1996) toy model for masses from 0.2 to 50 $M_\odot$. The black circle for MM1 indicates the values obtained by Beuther et al. (2002c) for this source, the black squares the values we derived as given in Tables 4 and 6. The white square indicates the location of the MM2 high-mass protostar. The total luminosity of the MM2 core is taken as an upper limit of the luminosity of the unresolved high-mass protostar.

protostar. Using the same dust properties (millimeter dust emissivity and average temperature) as in Motte et al. (2007) and inside a 0.13 pc size, the MM1 core would have a mass as high as 74 $M_\odot$, and would therefore be among the most massive cores of Cygnus X. With an equivalent $S_{20\,\mu\rm m}$ = 190 Jy at 1.7 kpc (distance of Cygnus X), it would be the brightest core not associated with a UC-HII region (see Fig. 7 in Motte et al. 2007). It is, however, not as bright in the mid-IR as the well-known AFGL 2591 source described by van der Tak et al. (1999). In the Motte et al. (2007) classification, MM1 is therefore a high-luminosity IR (or IR bright) protostar.

Except its nondetection in the mid- and far-IR ($S_{20\,\mu\rm m} \lesssim 2$ Jy), the properties of MM2 resemble those of MM1. It has a mass of 460 $M_\odot$ in a radius of 21 600 AU (core size of 0.22 pc) obtained with MC3D (Table 6), a still high bolometric luminosity of 2700 $L_\odot$, and it drives a powerful bipolar outflow. Using the same dust properties as in Motte et al. (2007), and inside a 0.13 pc, the MM2 core would have a mass of 45 $M_\odot$ and would therefore be among the 40 high-density cores of Cygnus X. In the Motte et al. (2007) classification, MM2 is a mid-IR-quiet massive protostar.

Observations of MM3 do not permit a definitive conclusion on its nature. Although it is massive with a flatter density profile (about 200 $M_\odot$ and p = 0.8, Beuther et al. 2002b) and no detected outflow, any mid-IR emission is confused due to the nearing confusing source detected by MSX and the presence of a bright IR filament in the background. At best, one can only propose that MM3 is a probable prestellar core.

One can also use the CO outflow energetics to further discuss the evolutionary stages of MM1 and MM2. Outflows are believed to be the best indirect tracers of protostellar accretion. Interestingly enough, while MM2 is not a bright IR source and is less luminous than MM1, its CO outflow is as powerful as the one of MM1. This is like Class 0 low-mass protostars, which on average have more powerful outflows than more evolved and IR-bright Class I objects. It has been interpreted by Bontemps et al. (1996) as due to a decrease in the accretion rate with time. Extrapolating these results to higher masses, we investigate in Fig. 16 how MM1 and MM2 place in the evolutionary diagram based on the energetics of CO outflows. The location of the low-mass protostars (Class 0 and Class I) is displayed with stars and is reproduced well by a toy model (dotted tracks) based on an exponential decrease in the accretion rate with time (see details in Bontemps et al. 1996) for stars between 0.2 and 2 $M_\odot$. Three additional tracks are given for M = 8, 20, 50 $M_\odot$. One can note, for instance, that, while the low-mass protostars reach a maximum luminosity that is higher than their final ZAMS luminosity (by a factor of 5 for 0.2 $M_\odot$ stars), the luminosities of massive protostars are always increasing. In this scenario, the dashed line would represent the location of the transition between Class 0 and Class I protostars, i.e. the location where half of the final mass is accreted (first black arrow symbols, second arrow symbols are for 90% of the mass accreted). If this can be extrapolated to high-mass protostars it indicates that MM2 is younger than MM1 and could host a high-mass Class 0 like protostar. The HMPO (star symbols) including MM1 and MM2 are not resolved well as individual collapsing objects. This is particularly important for MM2 for which the measured luminosity depends on its continuum fluxes in the millimeter range and therefore directly scales with the size of the region. The luminosity of MM2 should therefore be seen as an upper limit of the actual luminosity of the protostar. In this diagram, MM2 and MM1 are located in the area of the M = 20 $M_\odot$ track with MM2 having less than 50% of its final mass, and MM1 having about 50% of its final mass accreted. While the stellar embryo of MM2 is therefore certainly not yet a ionising star, MM1 could be hosting a

weakly ionizing stellar embryo of ∼10 $M_\odot$. This could explain why MM1 would appear as the brightest core in Cygnus X (in Fig. 7 of Motte et al. 2007), which is not yet associated with a UC-HII region.

The overall properties of MM1 and MM2 therefore provide us with a coherent picture of MM1 and MM2 hosting at least one high-mass protostar which are not yet creating a UC-HII region. MM2 hosts a certainly younger, and probably slightly less massive protostar, than MM1. The high-mass protostar hosted by MM1 is a good candidate for being just at the limit of switching on a new UC-HII region. In this scheme, well-known protostars such as AFGL 2591 would be slightly more evolved with an already formed UC-HII region and a much brighter flux in the mid-IR.

5.3. Density and temperature profiles from dust continuum

From the detailed 1D and 2D analyses of the continuum emission and of the optically thin molecular line modeling, we arrived at the conclusion that a 1D spherical geometry is enough to reproduce the molecular line emission. It is only to account for the mid-infrared emission that a 2D geometry is required. Our careful analysis showed that the 1D and 2D models were indistinguishable when it comes to modeling the molecular lines. This is actually not surprising since only a very small fraction of the total mass in the core is affected by the 2D inner flattening of the density distribution. Only 11 $M_\odot$ of the 660 $M_\odot$ of MM1 is found to be at $T > 100$ K. The bulk of mass is at much lower temperatures and does not contribute to the infrared emission (see Fig. 17).

Facing the same difficulty to reproduce the mid-infrared emission of massive protostars, van der Tak et al. (1999) adopted another strategy by using a 1D spherical model with a large inner cavity, which could let escape the infrared photons. Our results also validate this approach since it was a way to neglect the inner-dust contribution for the molecular line modeling. On the other hand, this approach tends to converge toward large sizes of the cores that are not observed. We believe it is more realistic to impose the sizes of the cores as observed in the dust continuum.

Finally, we note that the use of a self-consistent dust radiative transfer code such as MC3D is ideal for reducing the number of free parameters. On the other hand, it imposes some stringent hypotheses on the dust properties by requiring a full opacity curve for dust grains, from infrared to millimeter wavelengths. For instance, we use the MRN distribution of grains that is known not to take the real dust opacity in the millimeter range into account very well when ice mantles are present for cold and dense cores (Ossenkopf & Henning 1994). For SED modeling, this is not very important since dust emission in the millimeter range is optically thin. But it is important for mass derivation, we expect that the masses we derived are overestimated due to freeze-out onto grains. As a consequence the abundances could be underestimated accordingly. The resulting absolute uncertainty can be evaluated by directly deriving total masses from the 1.25 mm continuum fluxes of MM1 and MM2 in Table 5 using the mass determination by Motte et al. (2007) and the average temperatures obtained in Table 6. We get 200 and 114 $M_\odot$ for MM1 and MM2, respectively, which are ∼3.5 times less than with MC3D. This systematic effect is, however, a general concern and our resulting abundances are still directly comparable to results from most previous similar studies that used the same assumptions.

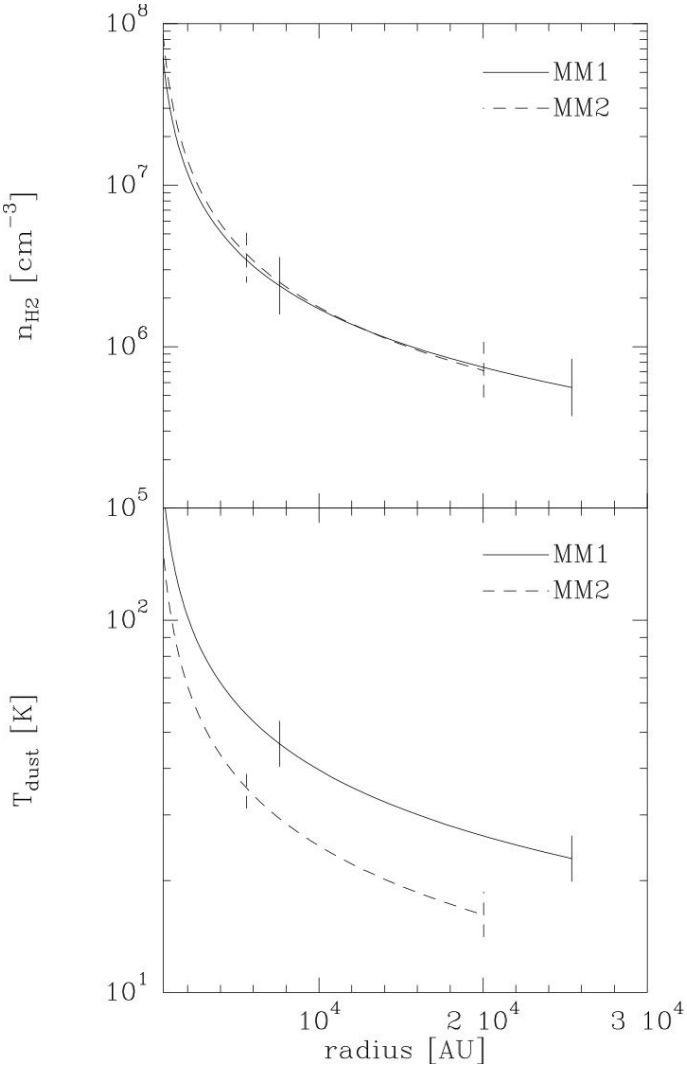

Fig. 17. Density (*top*) and temperature (*bottom*) profiles used in 1D for molecular line emission modeling of MM1 (plain) and MM2 (dashed). Intervals (vertical lines) represent where 90% of the mass is present in the models, hence what physical conditions are dominating line emission process of molecules observed.

5.4. Average abundances from molecular observations.

Modeling of MM1 and MM2 allowed us to derive absolute molecular abundances. The CS abundances we find, $X \simeq 0.5\text{–}1.0 \times 10^{-9}$, are typical values for this type of source (Pirogov et al. 2007). We note the same result for N_2H^+ where $X \simeq 3.5\text{–}6.3 \times 10^{-10}$ (Pirogov et al. 2003), HCO^+ with $X \simeq 2.3\text{–}5.1 \times 10^{-9}$ (van der Tak et al. 2000a), and finally $X(H_2CO)$ is in the wide, typical abundance range observed (Keane et al. 2001; Bisschop et al. 2007). All these results fit abundance ranges derived from standard chemical evolution modeling as made by Doty et al. (2002): X(CS) varying from 1×10^{-10} to 1×10^{-8}, $X(N_2H^+)$ from 1×10^{-12} to 3×10^{-10}, $X(HCO^+)$ from 1×10^{-11} to 6×10^{-9}, and $X(H_2CO)$ from 1×10^{-10} to 2×10^{-8}. Thus we conclude that our observations and models do not reveal any abundance anomaly compared to other massive protostellar objects and to chemical predictions.

5.5. Depleted CS abundance in the inner regions

The modeling of multiple line emission from a single molecular species enables us to probe physical conditions inside a source.

In our model, where no shocks are inserted, the main factor is thermal excitation. Modeling of CS transitions (E_{up}/k is equal to 7.0, 14.1, and 35.3 K for J = 2–1, J = 3–2, and J = 5–4) reveals that, for both MM1 and MM2 sources, the two lowest CS transitions are almost reproduced, whereas the highest one is stronger than observed (see Figs. 7 and 12). A lower abundance of CS in the inner regions could explain this discrepancy. Since the gas is cold and dense in basically the whole MM1 and MM2 cores, a significant depletion of CS onto the grains is expected (see Tafalla et al. 2002, and references therein). For the line modeling of the low-mass Class 0 protostar IRAM 04191, Belloche et al. (2002) had also to consider a significant CS depletion (by a factor of about 20) to reproduce the observed lines. The CS depletion is expected to still be significant, even for high-mass cores such as MM1 and MM2 because they have not yet formed a large hot-core region. Only a very small fraction of the total mass of MM1 is expected to be at $T > 100$ K. We conclude that CS depletion in the inner regions of MM1 and MM2 could be responsible for the too weak CS(5–4) emission that is not reproduced by our modeling.

5.6. H_2CO: a probe of physical and chemical interactions?

Our study clearly shows that the H_2CO emission we observed can be modeled with no radial variation of abundance. The test of an overabundance driven by a hot core ($T > 100$ K) does not show any significant improvement in line fitting. We can understand it from the low contribution in mass of the hot parts of MM1 and MM2 (resp. 11 $M_\odot$ and 3 $M_\odot$; see Fig. 17). Thus we conclude that H_2CO line emission does not show any hot-core contribution.

However the line emission from MM2 leads to a greater abundance of H_2CO than MM1, with a need for a hotter inner part, although it is the colder and the younger of the two sources. The line emission from MM2 could be affected by a significant contribution of outflow shocks in the inner envelope of the protostar. This idea is supported by the higher turbulent velocity observed in MM2 (v_T = 1.7 km s^{-1} in contrast to 1.0 km s^{-1} for MM1) and its internal para-to-ortho ratio greater than 1, suggesting recent chemical activity (Kahane et al. 1984) driven in these shocks.

5.7. Chemical evolution of high-mass cores

We finally wish to speculate that the chemical differences between MM1 and MM2 are related to their different evolutionary stages. The derived abundances, obtained with the same modeling process and radiative transfer code, show that X(CS) is 2 times higher for MM1 than for MM2, and 5 times lower than in the probably more evolved AFGL 2591 high-mass protostar, suggesting that the CS abundance might increase with time. Interestingly enough, the Johnstone et al. (2003) study of submillimeter sources in Orion was suggesting the same trend. The chemical models by Wakelam et al. (2004) actually predict such an evolution of the CS abundance in protostars: a constant production of CS is expected at low temperatures ($T < 100$ K), thus increasing the abundance with the source evolution. Moreover, when the hot core region develops, the release of CS from the grains may even increase the CS abundance more. This could be the case for the high abundances in AFGL2591 and in the sources observed by Hatchell & van der Tak (2003).

In contrast, $X(N_2H^+)$ is found to decrease with time; the N_2H^+ abundance inside AFGL 2591 shows a clear trend of decrease from MM2 to AFGL 2591: $X(N_2H^+)_{\rm AFGL\ 2591} = 0.1 \times X(N_2H^+)_{\rm MM1} = 0.05 \times X(N_2H^+)_{\rm MM2}$. This molecule hardly depletes on cold dust grains and is rapidly destroyed at warm temperatures. This behavior is not unique and has already been observed in high-mass protostellar objects (Reid & Matthews 2007). We suggest that the CS and N_2H^+, i.e. abundance ratio may be a good tracer of protostellar evolution, but more observations and modeling are required to test this hypothesis.

6. Conclusions

Here we summarize our conclusions on the massive protostellar objects MM1 and MM2 of the IRAS 18151–1208 region.

1. The three cores of the region, MM1, MM2, and MM3 are physically linked and were probably formed from a single parental cloud or clump.
2. We detected for the first time a CO outflow driven by MM2. It clearly establishes the protostellar nature of MM2. In contrast, MM3 does not show any outflow activity and is therefore most probably a pre-stellar core.
3. Following the evolutionary scheme discussed in Motte et al. (2007), MM1 is a high-luminosity IR (or IR-bright) massive protostar, while MM2 is an IR-quiet massive protostar.
4. We have established that, while an inner flattening of the matter distribution is required to reproduce the SED of MM1, a simple 1D spherical geometry is enough to model molecular line observations. In contrast, MM2 does not even require an inner flattening since it is not detected in the mid-infrared range.
5. A significant depletion of CS in the inner parts of the MM1 and MM2 cores is required to reproduce the observed CS line emission fully.
6. We find that the abundance ratio between CS and N_2H^+ could be a very good evolution tracer for high-mass protostellar cores hosting high-mass protostars.

Acknowledgements. We would like to thank Henrik Beuther for his useful and precise comments as referee and for kindly providing his 1.2 mm continuum map data of the region that we used for the figure of the whole region (Fig. 1). They both greatly improved the general content of this paper. We also thank Jonathan Braine and Nicola Schneider for their corrections.

References

André, P., Ward-Thompson, D., & Barsony, M. 2000, Protostars and Planets IV, 59
Aumann, H. H., Fowler, J. W., & Melnyk, M. 1990, AJ, 99, 1674
Belloche, A., André, P., Despois, D., & Blinder, S. 2002, A&A, 393, 927
Beuther, H., Schilke, P., Gueth, F., et al. 2002a, A&A, 387, 931
Beuther, H., Schilke, P., Menten, K. M., et al. 2002b, ApJ, 566, 945
Beuther, H., Schilke, P., Sridharan, T. K., et al. 2002c, A&A, 383, 892
Bisschop, S. E., Jørgensen, J. K., van Dishoeck, E. F., & de Wachter, E. B. M. 2007, A&A, 465, 913
Bonnell, I. A., Vine, S. G., & Bate, M. R. 2004, MNRAS, 349, 735
Bontemps, S., André, P., Terebey, S., & Cabrit, S. 1996, A&A, 311, 858
Cabrit, S., & Bertout, C. 1992, A&A, 261, 274
Caselli, P., Myers, P. C., & Thaddeus, P. 1995, ApJ, 455, L77+
Ceccarelli, C., Hollenbach, D. J., & Tielens, A. G. G. M. 1996, ApJ, 471, 400
Chernin, L. M., & Masson, C. R. 1995, ApJ, 455, 182
Chin, Y.-N., Henkel, C., Whiteoak, J. B., Langer, N., & Churchwell, E. B. 1996, A&A, 305, 960
Daniel, F., Dubernet, M. -L., & Meuwly, M. 2004, J. Chem. Phys., 121, 4540
Daniel, F., Dubernet, M.-L., Meuwly, M., Cernicharo, J., & Pagani, L. 2005, MNRAS, 363, 1083
Davis, C. J., Varricatt, W. P., Todd, S. P., & Ramsay Howat, S. K. 2004, A&A, 425, 981

Doty, S. D., van Dishoeck, E. F., van der Tak, F. F. S., & Boonman, A. M. S. 2002, A&A, 389, 446
Guilloteau, S., & Lucas, R. 2000, in Imaging at Radio through Submillimeter Wavelengths, ed. J. G. Mangum, & S. J. E. Radford, ASP Conf. Ser., 217, 299
Hatchell, J., & van der Tak, F. F. S. 2003, A&A, 409, 589
Hogerheijde, M. R., & van der Tak, F. F. S. 2000, A&A, 362, 697
Johnstone, D., Boonman, A. M. S., & van Dishoeck, E. F. 2003, A&A, 412, 157
Kahane, C., Lucas, R., Frerking, M. A., Langer, W. D., & Encrenaz, P. 1984, A&A, 137, 211
Keane, J. V., Tielens, A. G. G. M., Boogert, A. C. A., Schutte, W. A., & Whittet, D. C. B. 2001, A&A, 376, 254
Krumholz, M. R., Klein, R. I., & McKee, C. F. 2007, ApJ, 656, 959
Lucas, R., & Liszt, H. 1998, A&A, 337, 246
Mathis, J. S., Rumpl, W., & Nordsieck, K. H. 1977, ApJ, 217, 425
McCutcheon, W. H., Sato, T., Purton, C. R., Matthews, H. E., & Dewdney, P. E. 1995, AJ, 110, 1762
McMullin, J. P., Golap, K., & Myers, S. T. 2004, in Astronomical Data Analysis Software and Systems (ADASS) XIII, ed. F. Ochsenbein, M. G. Allen, & D. Egret, ASP Conf. Ser. 314, 468
Motte, F., & André, P. 2001, A&A, 365, 440
Motte, F., André, P., & Neri, R. 1998, A&A, 336, 150
Motte, F., Bontemps, S., Schilke, P., et al. 2007, A&A, 476, 1243
Ossenkopf, V., & Henning, T. 1994, A&A, 291, 943
Pirogov, L., Zinchenko, I., Caselli, P., Johansson, L. E. B., & Myers, P. C. 2003, A&A, 405, 639
Pirogov, L., Zinchenko, I., Caselli, P., & Johansson, L. E. B. 2007, A&A, 461, 523
Reid, M. A., & Matthews, B. C. 2007, ArXiv e-prints, 712
Schöier, F. L., Jørgensen, J. K., van Dishoeck, E. F., & Blake, G. A. 2002, A&A, 390, 1001
Schöier, F. L., van der Tak, F. F. S., van Dishoeck, E. F., & Black, J. H. 2005, A&A, 432, 369
Shakura, N. I., & Syunyaev, R. A. 1973, A&A, 24, 337
Shu, F. H. 1977, ApJ, 214, 488
Sridharan, T. K., Beuther, H., Schilke, P., Menten, K. M., & Wyrowski, F. 2002, ApJ, 566, 931
Tafalla, M., Myers, P. C., Caselli, P., Walmsley, C. M., & Comito, C. 2002, ApJ, 569, 815
Underhill, A. B., Divan, L., Prevot-Burnichon, M.-L., & Doazan, V. 1979, MNRAS, 189, 601
van der Tak, F. F. S. 2005, in Massive Star Birth: A Crossroads of Astrophysics, ed. R. Cesaroni, M. Felli, E. Churchwell, & M. Walmsley, IAU Symp., 227, 70
van der Tak, F. F. S., van Dishoeck, E. F., Evans, II, N. J., Bakker, E. J., & Blake, G. A. 1999, ApJ, 522, 991
van der Tak, F. F. S., van Dishoeck, E. F., & Caselli, P. 2000a, A&A, 361, 327
van der Tak, F. F. S., van Dishoeck, E. F., Evans, II, N. J., & Blake, G. A. 2000b, ApJ, 537, 283
van Dishoeck, E. F., & Blake, G. A. 1998, ARA&A, 36, 317
Wakelam, V., Caselli, P., Ceccarelli, C., Herbst, E., & Castets, A. 2004, A&A, 422, 159
Williams, S. J., Fuller, G. A., & Sridharan, T. K. 2004, A&A, 417, 115
Wilson, T. L., & Rood, R. 1994, ARA&A, 32, 191
Wolf, S., Henning, T., & Stecklum, B. 1999, A&A, 349, 839
Wood, D. O. S., & Churchwell, E. 1989, ApJS, 69, 831
Zinnecker, H., & Yorke, H. W. 2007, ARA&A, 45, 481